Effect of Morphological Features of Fuel Cell Cathodes on Liquid Water Transport

by

Valérie Raymonde Losier

B.Sc., McGill University, 2015

In Partial Fulfillment of the Requirements for the Degree of

MASTER OF APPLIED SCIENCE

in the Department of Mechanical Engineering

Effect of Morphological Features of Fuel Cell Cathodes on Liquid Water Transport

by

Valérie Raymonde Losier

B.Sc., McGill University, 2015

Supervisory Committee

Dr. Ned Djilali, Supervisor

(Department of Mechanical Engineering, University of Victoria)

Dr. Caterina Valeo, Departmental Member

(Department of Mechanical Engineering, University of Victoria)

ABSTRACT

Liquid water management in the cathode of polymer electrolyte membrane fuel cells (PEMFC) is crucial to efficient transport of gases and to maintaining electrochemical activity in the catalyst layer. Cracks and interfacial voids are typical of catalyst layers in operating cells, and are thought to affect water management and other transport properties such as gas diffusion and conductivity. This thesis investigates the effect of such morphological imperfections on liquid water transport using a combination of numerical techniques. Both the catalyst layer and microporous layer parts of the cathode are considered. The layers are first numerically reconstructed using data from advanced microscopy, and cracks, perforations and interfacial voids are created. Lattice Boltzmann simulations of the dynamics liquid water imbibition process are performed to study the effect of characterizing features of the cracks and interfacial voids such as aperture area, degree of protrusion, and tortuosity. The resulting liquid water distributions were then input into a pore scale model to characterize the effect of the morphological features on other transport properties, such as effective diffusivities and conductivities.

Larger crack apertures were found to increase liquid water uptake, and elongated cracks allowed for faster breakthrough at lower saturation levels. A notable observation is that short and large interfacial cracks have a higher liquid water uptake potential due to the lower effective capillary pressures. It was also found that elongated cracks aligned with the pressure gradient provide preferential pathway, and a capillary pressure increase that favours liquid water transport towards the membrane and mitigates flooding. The effective diffusivity increased for all crack protrusion depths, even for the wet catalyst layer, likely due to low liquid water saturation. The geometry with the most elongated crack showed a significant increase in gas diffusion under wet conditions, indicating that enhanced gas transport is achievable when liquid water removal is effective. Protonic and electrical conductivities decreased for all crack shapes due to higher contact resistance.

Contents

List of Tables

List of Figures

Nomenclature

Acronyms

BGK	Bhatnagar Gross Krook
CL	Catalyst layer
FIB-SEM	Focus Ion Beam Scanning Electron Microscopy
GDL	Gas diffusion layer
hcp	hexagonal close-packed
LBM	Lattice Boltzmann method
MEA	Membrane electrode assembly
MEM	Polymer membrane
MPL	Microporous layer
MRT-LBM	Multiple relaxation time lattice Boltzmann method
PEMFC	Polymer electrolyte membrane fuel cell
PNM	Pore network model
PSM	Pore scale model

PTFE	Polytetrafluoroethylene

Symbols

Ω	Solid angle
σ	Cross section
τ	Collision time [s]
$\mathbf{F}$	External force
$Q_f(f, f)$	Collision integral
α_c	Charge transfer coefficient
$\mathbf{\Gamma_t}$	Reaction flux
$\mathbf{\Gamma_t}$	Transport flux
δt	Time step [s]
η	Viscosity [m^2/s]
μ	Chemical potential [J/mol]
Φ	Flux
ϕ_m	Membrane potential (proton transport) [V]
ϕ_s	Solid potential (electron transport) [V]
ρ	Density [kg/m^3]
σ_m	Membrane conductivity [S/m]
σ_s	Solid conductivity [S/m]

$\mathbf{e}$	Discrete velocity
$\mathbf{F}_b$	Body force [N]
$\mathbf{g}$	Order parameter vector
$\mathbf{g}$	Order parameter vector
$\mathbf{j}$	Momentum [kg · m/s]
$\mathbf{M}$	Transformation matrix
$\mathbf{m}$	Velocity moment
$\mathbf{P}$	Pressure tensor [Pa]
$\mathbf{r}$	Lattice spacing
$\mathbf{r}$	Spacial vector [m]
$\mathbf{u}$	Velocity vector [m/s]
θ	Contact angle
φ	Local order parameter
c	Lattice velocity
c	Ratio between the lattice spacing and the time step
C_{H_2O}	Water vapour concentration [mol/cm^3]
$C_{O_2,ref}$	Reference oxygen concentration [mol/cm^3]
C_{O_2}	Oxygen concentration [mol/cm^3]
d	Diameter of the pore [m]

D_b	Bulk diffusivity [m^2/s]
D_{H_2O}	Water vapour diffusivity [m^2/s]
D_{Kn}	Knudsen diffusivity [m^2/s]
D_{O_2}	Oxygen diffusivity [m^2/s]
$f(\mathbf{r})$	Spacial distribution function
$f(\mathbf{u})$	Velocity distribution function
i_0	Exchange current density [A/m^2]
l	Length of the domain [m]
M	Mobility [m^2 /$(V \cdot s)$]
M	Molecular weight
N	Total number of particles in a system
p	Probability
R	Universal gas constant [$J/(mol \cdot K)$]
T	Temperature [K]
v	Mean molecular velocity [m/s]
X_{eff}	Effective transport parameter

Acknowledgements

I wish to thank my supervisor, Prof. Ned Djilali, for his support in choosing a project that interested and motivated me. I am deeply grateful for his insightful guidance. I truly appreciate the opportunities he created for me to flourish as a researcher and teacher.

A special thank you to Dr. Alireza Akghar who has shared with me his expertise on the modelling methods, and to Dr. Belaid Moa who provided generous support with the Westgrid Canada computing facilities.

I thank the Institute for Integrated Energy Systems (IESVic) for providing an enriched environment where I was exposed to various sustainable energy developments and for providing an inclusive atmosphere that greatly enhanced my graduate experience.

Of course thank you to my parents and Alex who continuously prove that they support me in any project I take on.

Chapter 1

Introduction

1.1 Motivation

Polymer electrolyte membrane fuel cells (PEMFCs) convert the chemical energy of a fuel, primarily hydrogen, into electricity in a clean reaction. They are suitable for portable applications due to the low operating temperatures and high efficiency. PEMFCs fuelled with hydrogen produced from renewable energy sources are a viable solution to reducing carbon emissions associated with the transportation industry, a prominent contributor to the current carbon crisis [5].

PEMFCs need to overcome two major challenges before they can be competitive enough to widely commercialize: cost and durability. The most significant part of the cost is the platinum catalyst for high electrochemical activity in the catalyst layer[6]. As it will be explained in detail in section 2.2, the mass exchanges in the fuel cell are as follows. At the anode, the hydrogen splits into protons and electrons, and the electrons pass through an external circuit to subsequently recombine with protons and oxygen at the catalyst layer of the cathode where clean water is produced as a result of the chemical reaction [7]. Assuring effective mass transport increases reaction rates and allows for lower platinum loading.

The polymer electrolyte membrane requires sufficient hydration to avoid dry-out and to attain high proton conductivity, however liquid water generated at the cathode can block access to reaction sites which impedes gas mixing and consequently decreases the efficiency of the device. An excess of liquid water in the porous layers is known as flooding and limits the electrochemical activity in the catalyst layer, therefore the removal of water in this region is essential to achieve optimal fuel cell performance [8].

Substantial advances in water management have been made by including a microporous layer (MPL) [9] and increasing the hydrophobicity of the porous layers [10]. Studies on interfacial effects between the catalyst layer, the MPL and the gas diffusion layer (GDL) demonstrated that interfacial cracks play an important role in mass transport processes and liquid water distribution in the cathode [11]. Cracks occur naturally through the manufacturing process [12] as well as during the operating cycles of the fuel cell due to the swelling and contracting of the porous layers [13] and other factors discussed in section 3.2. These cracks are typically considered mechanical defects, however some crack structures between porous layers could participate in water management [14].

Experimental studies have demonstrated that creating laser-cut perforated pores in the porous layers of the cathode offers a preferential path for liquid water and improves liquid water transport [15, 16]. This phenomenon is due to the lower capillary pressure and a reduced flow resistance in the perforated pore. If these constructed pores are properly engineered, they can be conducive to effective water removal and increased performance [17].

The impact of interfacial structures was analyzed by Han and Meng [18] by numerically creating perforations in the randomly generated MPL and GDL porous structures and simulating the liquid water transport using a two-dimensional, two-phase lattice Boltzmann method (LBM). The qualitative analysis conducted by Han and Meng agrees with the experimental observation that large cracks and interfacial structures provide preferen-

tial water transport pathways and can convenience water removal in flooding conditions. This numerical technique also enabled the authors to test various perforated pore orientations and arrangements to approach an optimally engineered interfacial pore structure which amplified the observed effects of controlled liquid water transport.

The focus of this work is to numerically model the effect of cracks on liquid water transport and other transport properties such as gas diffusion and conductivity through a lattice Boltzmann method and a pore scale model. The computational geometries are obtained by FIB-SEM reconstruction, then perforated pores of various structural geometries are introduced in order to simulate gas and liquid water transport through the porous layers using a three-dimensional LBM. The LBM, which solves the discrete Boltzmann equation, is the method of choice due to its ability to simulate multiphase flows. The model uses a multiple relaxation time collision operator and is based on the diffuse interface theory [19].

Gas diffusion and conductivity are strongly dependent on the nano and micro structure of the porous layers [20], therefore to obtain a full understanding of the processes in the PEMFC when cracks are involved, their effect on mass transport is modelled. The computational modelling of the two-phase flow through the micro porous geometries of the catalyst layer is achieved using a high resolution pore scale model [4]. A reconstructed three dimensional catalyst layer is used, and the finite volume method is used to discretize the governing flux equations for mass transport and electrochemical reactions in the reconstructed porous domain.

1.2 Organization

The topics discussed in each chapter are listed as follows.

Chapter 2 contains a review of liquid water management issues in PEMFC, techniques

used to mitigate the issues in the cathode, and a discussion on modelling liquid water transport in the porous media.

Chapter 3 describes the origin of cracks and morphological defects in the fuel cell and discusses their effect on performance. The characteristics of cracks observed in the cathode which are used as inspiration for the shape of the computationally implemented cracks in the study are presented.

Chapter 4 gives an overview of the numerical techniques including the reconstruction process to obtain a computational geometry of a realistic cathode, the lattice Boltzmann method used to model liquid water transport, and the pore scale model which models electrochemical activity and the mass transport in the cathode.

Chapter 5 presents the details of the experiments and a discussion of the results.

Chapter 6 concludes the work and gives an outlook on future work.

Chapter 2

Liquid water management in PEMFC cathodes

2.1 Overview

This chapter discusses the issues of water management in the cathode of PEM fuel cells. The discussion begins with an overview of the mechanics of the fuel cell and the chemical reactions which lead to water generation. The different facets of the impact of liquid water on fuel cell performance is then explored, followed by techniques used to mitigate these water management issues such as increasing hydrophobicity in some layers, adding a microporous layer between the catalyst layer and the gas diffusion layer, and changing the flow field design of the current collector plates. The chapter concludes with a discussion on the challenges of numerically studying liquid water dynamics and the method used in this work is introduced.

2.2 Liquid water generation

The hydrogen fuel is supplied across the area of the fuel cell using flow plates at the anode of PEMFC while oxygen or air is channelled at the cathode. At the anode the hydrogen splits into protons and electrons, with the help of a platinum catalyst. The anode reaction is expressed in equation 2.1. The overall reaction is illustrated in figure 2.1.

$$\mathrm{H_2} \longrightarrow 2\,\mathrm{H^+} + 2\,\mathrm{e^-} \tag{2.1}$$

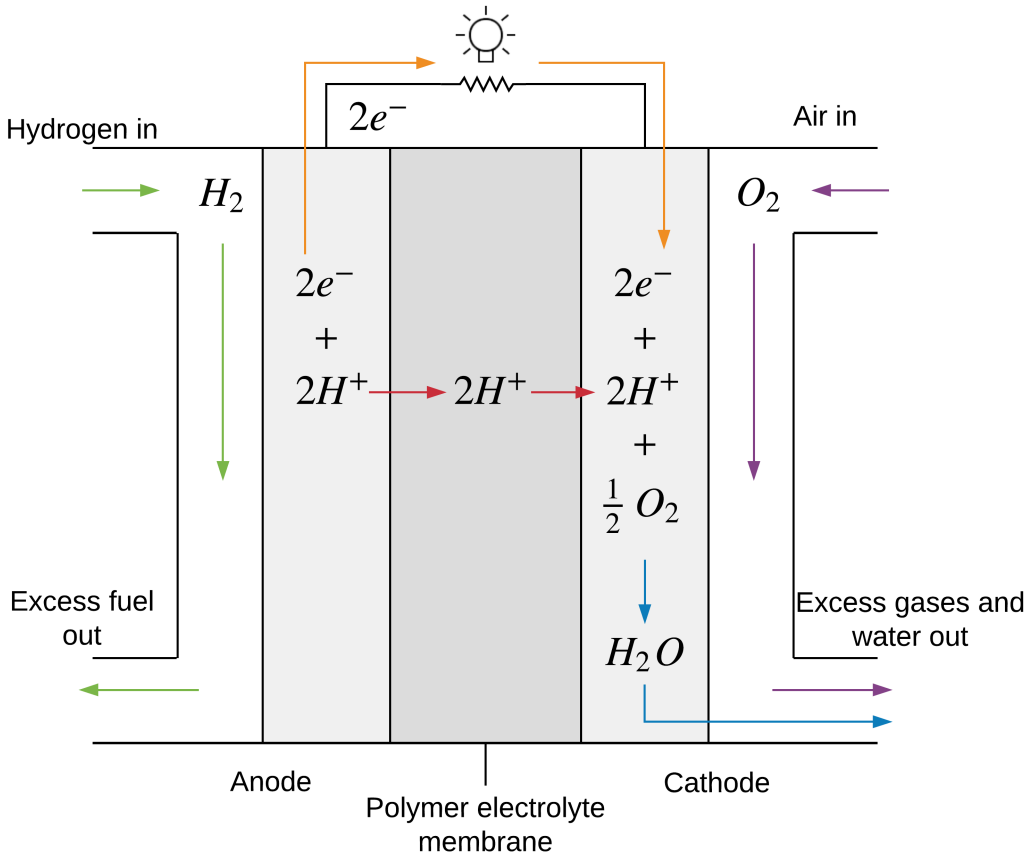

Figure 2.1: Mass transport in PEMFCs.

The electrode membrane is composed of a polymer backbone and is sulfonated with hydrophobic acid clusters which permit a high proton conductivity when adequately hy-

drated [21, 22]. The membrane has a high band gap which isolates the electrons so they pass through an external circuit where the electrical energy is provided.

The protons and electrons move to the catalyst layer, a porous structure with a thickness of 5-30 μm which consists of carbon particles with a radius averaging 50 nm and platinum particles, all covered by an ionomer. The protons travel through the ionomer, the electrons are conducted in the carbon particles and they are recombined with the oxygen at an active site with the aid of platinum as catalyst. The oxygen reaches the active site by diffusing through the pores from the cathode flow channel. The product of this chemical reaction is clean water [8]. The chemical reaction and species transport in the cathode is demonstrated in figure 2.2. The chemical reaction for the cathode and the overall reaction are expressed in equations 2.2 and 2.3 respectively.

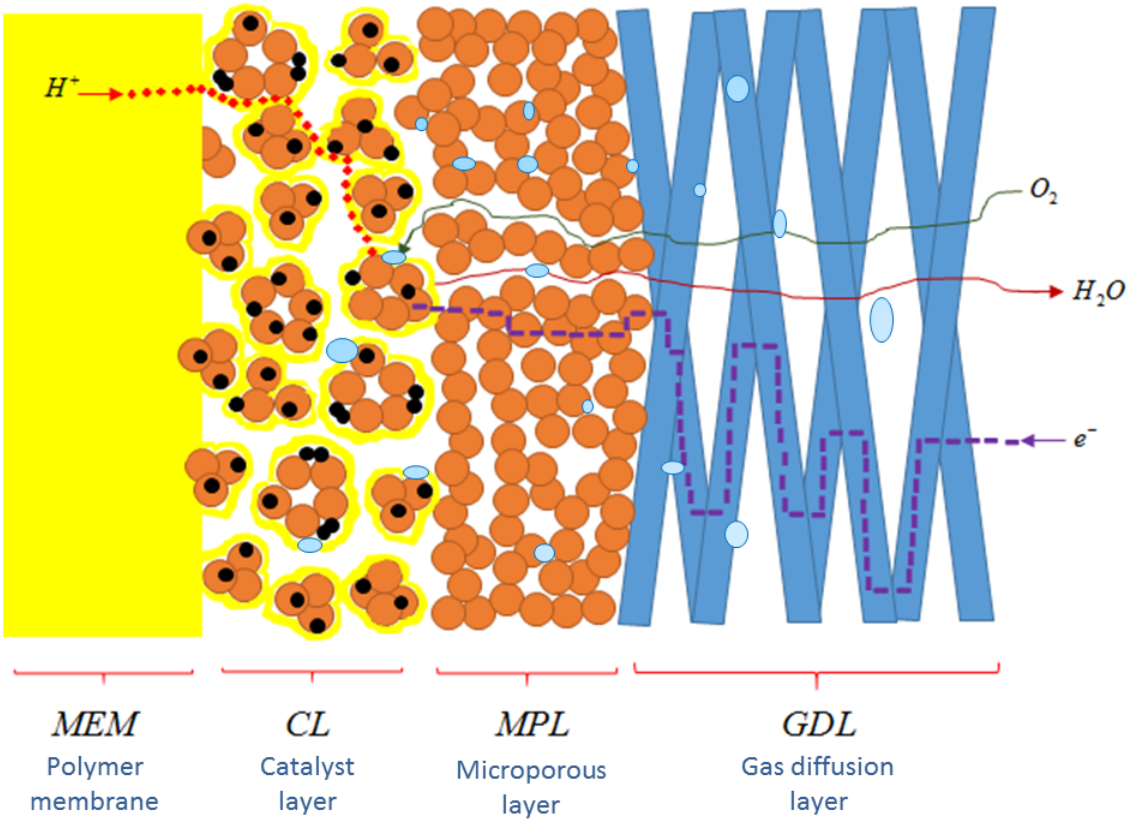

Figure 2.2: Schematic of mass and charge transport dynamics in the cathode of a PEMFC.

$$\frac{1}{2}\mathrm{O_2} + 2\,\mathrm{H^+} + 2\,\mathrm{e^-} \longrightarrow \mathrm{H_2O} \tag{2.2}$$

$$\mathrm{H_2} + \frac{1}{2}\mathrm{O_2} \longrightarrow \mathrm{H_2O} \tag{2.3}$$

The water leaves the catalyst layer and moves toward the microporous layer (MPL) and the gas diffusion layer (GDL) and eventually leaves via the flow channels in the current collecting plates.

2.3 Impact on performance and transport properties

The efficiency of the device relies on the efficient transport of gases and water through the porous layers of the fuel cell. It was experimentally shown that electron and proton transport are affected by water vapour transport [8], and the impact of liquid water transport should also be further studied.

Water is transported in the electrolyte from the anode to the cathode through electro-osmotic drag, due to water molecules having a polar attraction to the positively charged protons [22]. Water is also generated in the cathode through the oxygen reduction reaction (ORR) and often condenses due to the low operating temperatures of PEM fuel cells [23]. Liquid water is removed from the catalyst layer by evaporation and transport by capillary action towards the GDL and flow channels. If the uptake rate of liquid water in the cathode is larger than the rate of liquid water removal, excess water accumulates, referred to as flooding [24]. Common conditions which lead to flooding include operating at high current density such that water is generated faster than the media is able to remove it, or operating under low temperature and low gas flow rates which lead to condensation of the water vapour and low current densities.

Flooding in the cathode blocks pores in the CL and GDL which reduces gas transport.

Blocked pores in the catalyst layer limit access of oxygen to platinum sites, thus reducing the electrochemical activity [8, 23]. Many experimental studies of the polarization curve, a plot showing the relation of the cell voltage with respect to current density, show that performance is negatively affected by flooding [23]. The performance curve are steeper for cells under flooding conditions and begin to drop at lower current densities. The blockages in the cathode can lead to non-uniform distribution of reactants across the cells in the stack leading to variable and unpredictable performance [25].

However as discussed in the previous section, the ionic conductivity of the polymer electrolyte membrane is optimal when humidified. High water removal rate in the cell can cause membrane dehydration, and the consequential ohmic losses reduce efficiency, increase temperature and can accelerate membrane degradation such as thinning and the formation of pinholes [25, 23]. These issues underscore that a delicate balance of water during operation is critical to ensure optimal performance of fuel cells.

Water also plays an important role on degradation due to an imbalance of reactants. The hydrogen reaction at the anode is unaffected by flooding in the cathode and will continue to deliver high current, however if active sites are blocked at the cathode and the protons and electrons cannot be consumed, the potential difference will increase. In locations of fuel starvation at the cathode, the high current causes an acceleration of carbon corrosion and platinum dissolution [23, 21]. This reduction in carbon support and catalyst reduces the connectivity of the conducting materials to the active sites and decreases performance [26].

Additionally, for use in subfreezing temperatures, the inefficient removal of liquid water can lead to mechanical degradation if the water solidifies and expands to form ice. Efforts are made to remove water from the system by purging and applying external heat to the fuel cell before shutdown with minimal energy [8].

2.4 Water management techniques

Without efficient water management, performance is decreased due to flooding of the cathode. Liquid water removal involves phase change and transport through the porous layers to be removed by the flow plate channels. The diffusion media which have a higher porosity than the catalyst layer provide support for the thin catalyst layer, disperse gases, heat and provide a path for electrons. They also serve to remove water from the catalyst layer to the flow channels through capillary effect since water will preferentially fill larger pores in a hydrophobic media. The two-phase dynamics observed suggest that water transport is strongly affected by the capillarity and wettability of the GDL [10] as well as the pressure in the cathode [27]. These characteristics can be used to improve the water management aspect of the diffusion media and are discussed in this section.

Hydrophobicity

The gas diffusion layer can be treated with hydrophobic material such as polytetrafluoroethylene (PTFE), commonly known as Teflon, to change its wetting properties [25]. When porous layers are coated with hydrophobic materials, liquid water tends to decrease its surface area with the solid, which increases the contact angle [12] and facilitates removal of liquid water in the porous layers.

However excessive PTFE loading can lead to entry pressure in the MPL capillaries which are too high which discourages water transport from the catalyst layer to the GDL and lead to flooding [25]. Controlled patterned hydrophobicity could dedicate separate pathways for gas transport, and others for liquid water transport [28].

To simulate the effect of hydrophobicity on liquid water transport, numerical simulations adopting the Shan-Chen multi-phase approach lattice Boltzmann method were performed with randomly generated geometries with a prescribed porosity [10]. The wettability of the GDL was varied and the simulation indicates that as the hydrophobicity increases

the amount of liquid water in the porous layers decreases

Experimental studies were also conducted on PTFE treated and non-treated gas diffusion layers [29]. Compared to the the fuel cell with the PTFE treated GDL, the polarization curve for the fuel cell with untreated GDL shows a steeper decline in potential at lower current densities which suggests that flooding occurred. These results show that better performance was obtained with the PTFE coated layer.

Unfortunately, as observed during lifetime tests, the operating conditions and the interaction with water affect the hydrophobicity of the material, reducing fuel cell performance over time [23].

Microporous layer

The microporous layer (MPL) is a widely used fine pore structure located between the catalyst layer and the gas diffusion layer (GDL) and provides effective water transport. The GDL is composed of carbon fibres, while the MPL is composed of carbon particles, coated with PTFE as well [30].

A recent numerical study by Kim et al. [10] explores the effect of increasing the MPL thickness through lattice Boltzmann simulations, which suggestis that the GDL has a lower water content when a thicker MPL is used. Weber et al. [31] performed two dimensional two-phase numerical simulations and attributed the increase in performance with the MPL to improved water management and reduced ohmic losses. The reduction in ohmic losses is due to the improved interfacial contact between the catalyst layer and the diffusion media.

Experimental studies by Qi et al. [32] showed that MPLs provide benefits such as preventing the catalyst from penetrating in the GDL, increasing contact between the catalyst layer and the diffusion media as well as improving water management. The authors suggested that the microporosity and uniform pore distribution affected were the main factor in the MPL's impact on water transport. Bresciani et al. [27] showed that the MPL causes

the breakthrough pressure to increase and hypothesized that since the pore radius is lower than in the GDL, capillary pressure must reach higher levels in the CL in order to enter the diffusion media. This aids the MPL in focusing liquid water in a few injection spots into the GDL [8]. Nishiyama et al. [33] experimentally showed that under wet conditions, the cell where the MPL morphology and wettability yielded the highest capillary pressure in the MPL had the highest performance due to lower liquid saturation.

The MPL is understood to have larger saturated vapour pressure than the GDL due to the lower porosity which makes condensation and flooding less likely in hydrophobic media[25]. The water is required to build up pressure before entering the MPL which also allows for pressure to build up in the GDL and simultaneously push water towards the membrane as well as encourage water transport in less hydrophobic pores towards the flow channel where the water is expelled [25, 34].

Flow field design

Once liquid water reaches the flow field plates, it must be removed from the system. The flow field channels are responsible for supplying oxygen to the cathode and evacuate the water. The flow field plates are crucial for electron transport and their contact resistance with the GDL must be minimized.

Liquid typically condenses and accumulates under the land at the interface [8]. The geometry of the channels is important as water moves with more ease into a flow channel with round land edges compared to right angled edges. The water in the channels are flushed out by gas pressure build up.

Flow field design can mitigate channel clogging [16, 35]. A flow field design which is typically ineffective is the conventional flow field where the channels are straight and parallel. In this case diffusion dominates the transport process, therefore at low gas pressures water accumulates and this leads to a non uniform supply of gas to the cathode [25]. In

contrast, a serpentine flow field design which has long channels with many turns establishes a strong pressure drop with respect to neighbouring channels. This features encourages the gas to exit the channel in regions of high pressure and passing through the GDL toward the regions of low pressure. The enhanced gas flow effectively encourages transport of the liquid water out of the electrode [25].

2.5 Numerical study of liquid water dynamics

Modelling techniques for PEM fuel cells have evolved from one dimensional single phase flow to three dimensional multi-phase flow [25].

Models applying the computational fluid dynamics method (CFD) coupled with electrochemical reactions have become very advanced [36]. However, in this approach the water phases are modelled individually with diffusion and challenges remain in modelling phase change interaction between the phases which limits the reliability in predicting water transport and flooding [24, 31, 37].

A popular two phase flow pore-scale model for porous structures is the pore network model (PNM), based on local pore dynamics where transport of liquid water is dominated by capillary action [38, 30]. The model allows one to study the path of least resistance, the behaviour of clusters towards a path for breakthrough, and the behaviour of the system once breakthrough is achieved. A significant limitation to the PNM is the simplification of the flow processes which does not allow for viscous coupling [39].

The lattice Boltzmann method (LBM) is used in this work to because it can model multi-phase fluid transport with interfacial dynamics effects from capillary and viscous forces [40, 41, 42]. The density distribution function of velocity and of the order parameter, defined as the density difference between the liquid and gas phase, are evaluated at each node in the computational domain based on the free energy model by Swift et al. [41].

Based on the Shan and Chen [43] approach for interaction between particles, a collision operator models surface tension. In addition, the contribution by Nui et al. [19] allows for modelling a system with high density and viscosity ratios which typically allow for better modelling of the gas diffusion layer, is of essence in modelling water transport in a system comprised of a catalyst layer and a microporous layer with cracks. An overview of the MRT-LBM method applied in this work can be found in section 4.3.

Chapter 3

Structures in PEMFC cathodes

3.1 Overview

Interfacial topology between the layers of the fuel cell affect thermal resistance, contact resistance, and mass/charge transport. The multifaceted impact of structures at the MPL and CL interface have not been extensively studied [1]. Imperfections such as fractures and delaminations are inevitable in fuel cells, and the circumstances under which they form are described in the first section of this chapter. The known effect of cracks on performance and open questions are then discussed, and the types of cracks found at the MPL|CL interface which inspired the morphology of the cracked geometries used in the simulations of this work, are presented in the final section.

3.2 Mechanical defects in PEMFC

Defects in the porous layers arise during the fabrication and the operation process [44]. The conditions leading to their formation is discussed in this section, as well as current efforts to numerically model their propagation in fuel cells.

3.2.1 Degradation

Freeze and thaw cycles which occur in sub zero environments are known to induce cracks due to the stress caused by the expansion of residual of water in the pores as it freezes [1, 44]. Oszcipok et al. [45] conducted experimental studies to measure the impedance and obtain polarization curves of fuel cells operating in freezing conditions and unveiled the degradation caused by ice formation.

Qiu et al. [46] observed the formation of cracks after they performed 300 accelerated relative humidity cycles as well as 40 start/stop cycles. This is explained due to the temperature rises and relative humidity increase during operation, which cause the layers to swell. Under high current densities the temperature of the cell is higher and the relative humidity is lower than at low current densities. The ionomer uptakes water and swells under high water content, which can cause stresses and microcracks in the ionomer when the system dries [47]. Due to the varying composition, nonuniform water content and temperature, the layers have different expansion ratios and interfacial cracks form at the interfaces through the start/stop cycles [23].

Mechanical loads also play a key role in the formation of cracks. The contact points of the diffusion media with the flow plates are regions of high stress in a fuel cell stack and a gradient in pressure, or variable pressure distribution can enhance stress in some regions [23].

Large pores in the gas diffusion layer are hypothesized to produce cracks in the microporous layer due to a lack in mechanical support [2]. Other processes that can lead to morphology changes are corrosion of the carbon particles acting as catalyst support and ionomer degradation [8], however it is not clear if such structural changes affect crack formation [23].

3.2.2 Manufacturing

Fractures occur during manufacturing due to the drying of the hydrophobic coating. Some methods used in manufacturing can partake in the formation of cracks, voids and interfacial gaps. The manufacturing process is done layer by layer. First a MPL is formed by rolling, spraying, screen-printing, or brushing a viscous solution which includes carbon powder onto a hydrophobic carbon cloth [48]. It is then dried, chemically treated and washed to remove the salts that were used to form the viscous mixture. After drying, the pores are formed by sintering under high temperatures [49]. The gas diffusion electrode method to assemble the gas diffusion media, catalyst layer and polymer membrane first involve adding the catalyst solution trough brushing, blade or spray onto the diffusion media, which is set on a hot plate. For effective proton conductivity between the polymer electrolyte and the catalyst layer, a solution such as Nafion is sprayed on the catalyst. Once the electrodes are assembled, they are thoroughly rinsed with hot water and dried and hot pressed onto the polymer membrane. An alternative technique to assemble the electrode is to apply the catalyst ink to a sheet for support, then hot press the catalyst layer to the polymer membrane. The sheet is then peeled off the catalyst layer and hot pressed to the diffusion media [50].

The high temperatures used to assure electrical contact between the layers induces fractures due to the varying expansion ratios related to temperature [48]. The manufacturing methods used to assemble the layers also affect crack distribution and size. For example, Yan et al. [51] showed that the screen-printing method for applying the MPL yields smaller cracks than the spraying process [51]. Aditionally Aoyama et al. [50] observed that there were fewer interfacial gaps between the polymer membrane and the catalyst layer in the fuel cells assembled by the decal transfer method than by the gas diffusion electrode method, however there were more gaps at the catalyst layer and gas diffusion media interface for the system assembled using the decal transfer method. In both cases, the interface

assembled through hot pressing yielded more interfacial defects.

In systems where fibres from the GDL protrude into the MPL, an elevated crack density is observed [48], so interfacial roughness is also important to correct.

Materials, chemicals and physical procedures can be altered in order to reduce crack formation in the membrane electrode assembly. For example, to mitigate the formation of defects during drying, an applied pressure-controlled technique can be used to reduce the drying rate at high temperatures [52].

The size of the pores in the catalyst layer was observed to be proportional to the thickness of cracks [53]. One of the factors influencing the pore size is the duration of mixing the solution and it was observed that the longer the solution is mixed, the fewer cracks emerge in the assembly process [53]. The chemical composition in the catalyst layer solution can be adapted to impede the agglomeration process effectively reducing pore size, and to reduce interfacial tension with the MPL during the drying process by varying viscosity, which would reduce the volume of cracks [44]. Additionally, as experimentally determined by Suzuki et al. [54], the materials used are critical. The authors compared carbon black, traditionally used as carbon support, and multi-walled carbon nanotubes (MWCNTs) blended in catalyst ink for catalyst layer fabrication. The porous structure with MWCNT, yielded lower porosity, larger pores, and fewer cracks.

3.2.3 Modelling the formation of cracks

The cracks formed in the microporous layer from the drying and sintering process share many similarities with clay-rich soils that are subjected to extreme drying such as intersecting angles and relative area through the cracks [37]. The crack patterns and evolution can therefore be modelled stochastically using models for fragmentation of drying soil [55] and cohesive zone models which considers the effect of external forces [56].

Banan et al. [13, 14] implemented a a two-dimensional finite element model based on

cohesive zone theory to study the effect of relative humidity and heat cycles as well as vibrations on the propagation of cracks in the membrane electrode assembly. The simulations uncovered that relative humidity and heat cycling primarily led to significant crack propagation, while the vibrations mainly caused delaminations at the interfaces.

Incorporating the effect of water in the system in crack propagation models should be considered for fuel cells. Fowler and Scott [57] have proposed a single phase multiphysics elastohydrodynamic model for the propagation of a crack filled with a liquid in a porous medium. The model, governed by elastohydrodynamic equations for crack propagation and a pore pressure field, was intended for soil systems such as drainage networks forming in porous rocks and hydraulic fractures formed in oil drilling. The system differs from fuel cells primarily in the acting forces since in their model gravity acts in the direction of crack propagation.

These models require nodes from which cracks propagate. The interfacial structures resulting from the manufacturing process have not yet been considered as an initial state for such models [1] and should be studied in the future.

3.3 Effect on performance

Mechanical defects have a multifaceted impact on the performance of fuel cells since a reduction in contact area and water pooling affect liquid and gas transport, temperature conductivity as well as contact resistance [58].

To experimentally compare the performance of fuel cells with negligible and significant defects, Manahan et al. [11] have introduced cracks in the catalyst layer at the interface with the microporous layer to occupy 6% of the interface. Under wet and dry conditions, 100% relative humidity and below 70% relative humidity, respectively, gas diffusion was higher by 0.5% in the fuel cell with cracks. The polarization curves were also obtained

for the cracked fuel cell and the authors observed that the wet and dry conditions affected the regions of low, intermediate and high current densities differently. In the region of very low current density, the cracked system performed better under dry conditions by producing a 1.6% higher voltage. However, for moderate current densities, the fuel cell under wet conditions outperformed the experiment under dry conditions by 2.5%. Finally in the region of high current densities the cracked cathode provided higher voltage under dry conditions by 38.2%. The authors also compared the fuel cells with negligible and significant cracks under wet conditions and found that the cracked system performed worse under low and moderate current density conditions, possibly due to lower percentage of electrochemically active area caused by the removal of the platinum from the carbon and ionomer interface [1]. Conversely, the cracked system performed slightly better than the non-cracked system under high current density, possibly due to superior water management in flooding conditions.

Similar experimental studies were conducted by Gerteisen et al. [16] where large straight pores of diameter 1μm and spaced 1mm apart were produced in a GDL using laser beams. The fuel cell with the perforated GDL performed better than the unaltered fuel cell at high current density, increasing the limiting current density by 8% under dry conditions and by 22% under wet conditions. The improvement of the overpotential also suggests less limitation on oxygen transport. This study shows the potential of using cathodes with engineered perforations during the manufacturing process in order to enhance water management.

The crack density and area of the cracks seem to increase proportionally with hydrophobicity in the MPL [37, 59]. The small hydrophobic pores and high capillary pressure in the MPL discourage condensation, so the water transport is typically in vapour form and condensation occurs in the larger pores of the GDL. However, in hydrophobic structures, larger pores encourage condensation and water uptake due to capillary effect and reduced flow

resistance. The cracks would then offer liquid water preferential pathways[18], enhance water removal from the catalyst layer, encourage fingering in the GDL due to discrete injection spots and enhance liquid and gas transport in the GDL [37, 27, 27]. This phenomenon is speculated to improve water management at high current densities [38]. While water preferentially enters large cracks since the capillary pressure in the cracks are larger than in nanopores, the gas can travel in the unobstructed smaller pores. Alternatively, the preference of water to travel to large pores can also cause an accumulation and trapping of water in cracks [44].

Pore network modelling by Ma et at. [37] showed that when 1% of an MPL is cracked the permeability of the cell can increase by 2 to 5 orders of magnitude, depending on the area of the crack. Han and Meng [18] numerically studied the effect of interfacial structures on liquid water transport by creating perforations in the porous structure and simulating the mass transport using a two dimensional two-phase lattice Boltzmann method. The porous structure of the MPL and GDL was randomly generated to obtain a desired porosity and average pore size. Four different perforated pore geometries were studied: without perforations, with one large perforated pore oriented perpendicular to the interface, with three perforated pores of the same orientation and size, and finally with a large pore parallel to the MPL and GDL interface and a second perforated pore perpendicular to the interface. In the base case with no perforated pores, liquid water appears to chaotically penetrate through the pores and small droplets emerge at multiple locations along the top channel. For the case of the induced single pore, the water preferentially travels through the perforated pore and a single large droplet emerges at the end of the crack. In the case of the three perforated pores, the water moves faster in the large pores with low liquid saturation in the porous region. In the final case, the water first occupies the crack along the interface, then travels along the GDL in the perpendicular crack. In this case, the liquid water travels almost solely through the perforated pores.

Medici and Allen [38] applied a two-dimensional two-phase flow network model to a geometry composed of cylindrical tubes and random pore size. The simulations show that while cracks encourage fingering, the crack reduces the capillary pressure of the MPL and the injection pressure of the water into the GDL is similar to a porous transport layer without an MPL [38].

The contact resistance model used by Swamy et al. [58] which takes surface profile information from optical profilometry suggests that large interfacial gaps due to imperfect contact between the CL and MPL lead to water accumulation and store 6-18% of the water in the system. This would limit gas transport as discussed in the previous chapter. The low surface contact between the layers would obstruct the electron path and increase contact resistance [1, 20].

Cracks in the GDL, which arise as clamping pressure is increased, affect the pressure drop in the channel as discovered by Haase and Rauber [60].

Cracks in the electrodes curtail structural integrity and durability, so further studies should take place to understand the impact of realistic imperfections including cracks, holes and surface roughness on water flow, oxygen transport and performance [34, 48].

3.4 Cracks observed in the cathode

Several experimental studies have been conducted to visualize the cracks present in the cathode. This section is dedicated to discussing characteristic morphological features of different types of cracks.

Hizir et al. [1] have used scanning electron microscopy (SEM) and optical profilometry with sub-micron resolution to characterize the MPL and CL surfaces. As observed in figure 3.1, the MPL has a higher surface roughness than the CL. The roughness and interfacial structures have a height on the order of $10\mu m$ and can accumulate water. This was corrob-

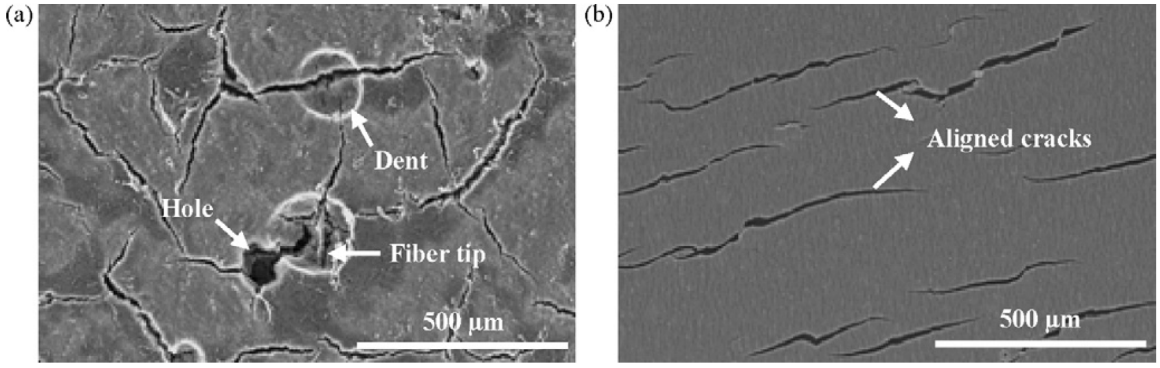

Figure 3.1: SEM image of (a) microporous layer surface (b) catalyst layer surface. Figure reprinted from Hizir et al. [1] with permission from Elsevier.

orated by a similar optical profilometry experiment performed by Swamy et al. [58] where they calculated a peak average of surface roughness of 25μm for the MPL, and 10μm for the CL. They calculated the width of the gaps are around 20μm.

Deep and half cracks are present in the MPL and CL. The cracks in the CL are described as thin ribbons and are generally parallel. Hizir et al. [1] calculated the crack density of the surface area of the CL to be $3.4 \pm 0.2\%$, and the crack width is seemingly constant at about 15μm in the centre of the cracks. In contrast, elongated cracks in the MPL which can span the whole length of the layer have random orientation, irregular width, and can have thicknesses of up to 60μm as observed in figure 3.2. Holes occur on the surface with diameters of about 100μm. The crack density of the MPL surface was observed to vary between 2.8% and 8.9% depending on the frequency of holes in the region. SEM images like the one presented in figure 3.2 show a transition region with MPL media and GDL fibres. The elongated crack in the MPL of figure 3.2 suggests that some cracks can extend into the MPL and GDL interface [1]. These observations were corroborated by the SEM experiments performed by Martinez-Rodriguez et al. [61] where they reported the width of MPL cracks to be between 4.4μm to 32μm and that the volume of the cracks increase proportionally to the hydrophobicity in the MPL.

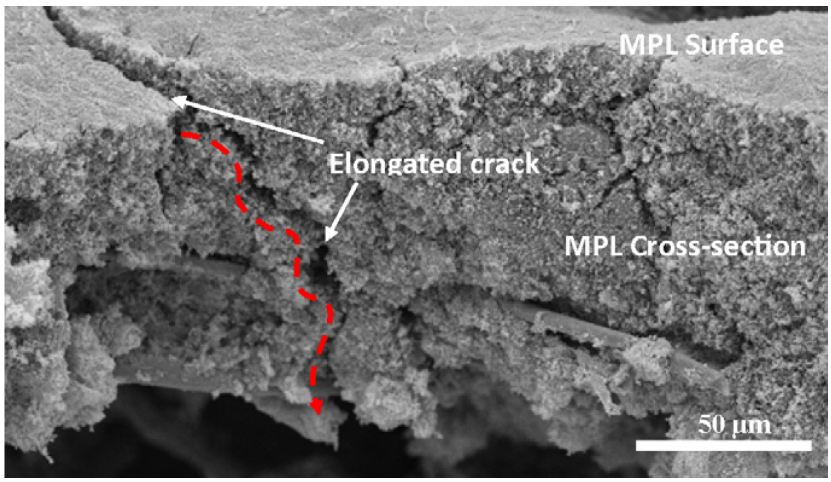

Figure 3.2: Cross-sectional SEM image of a microporous layer. The gas diffusion layer can be seen at the bottom and the arrows indicate the flow path. Figure reprinted from Hizir et al. [1] with permission from Elsevier.

Prass et al. [2] have also conducted experimental studies to characterize the MPL and CL interface at the cathode. X-Ray micro computer tomography (X-mCT) was used to image at high resolution on the order of micrometers. The electrode was assembled using the decal transfer method and the results revealed that large interfacial gaps were commonly found near elongated cracks as observed in figure 3.3.

3.5 Summary

As discussed in this chapter, there are multiple possible causes for the formation of imperfections in the electrodes. The source of the degradation and the manufacturing techniques each produce cracks and interfacial structures of distinct characteristics.

The effect of cracks on performance is multifaceted and seems to improve performance through enhanced water management under wet conditions and high current density, but reduce performance under dry conditions due to an increase in contact resistance.

Previous numerical and experimental studies which aimed to uncover the role of cracks on water transport and performance have mainly focused on elongated and thin cracks.

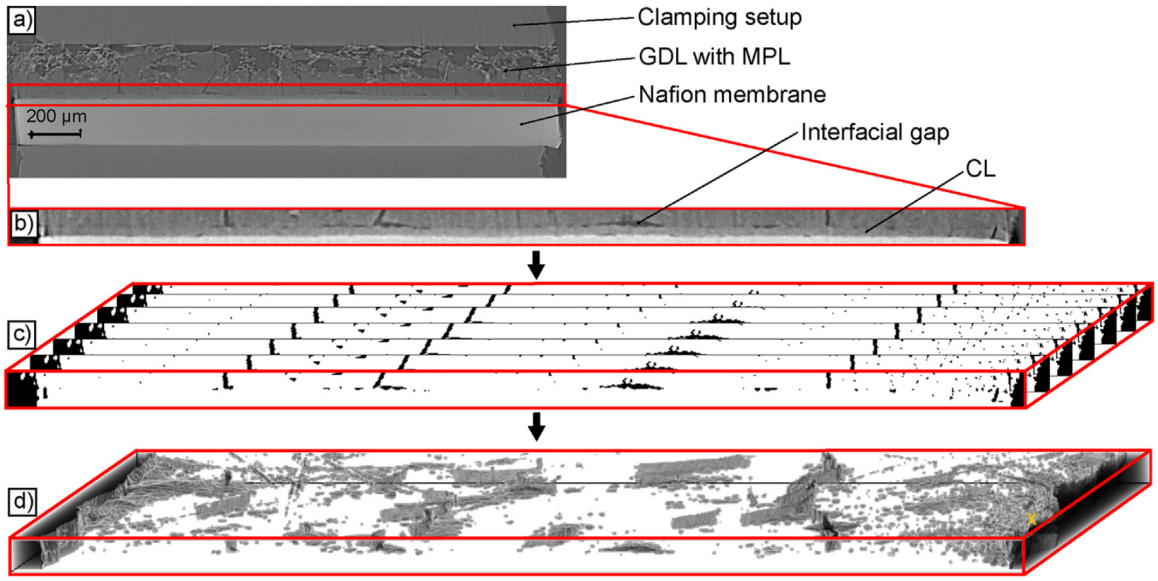

Figure 3.3: X-Ray micro computer tomography (X-mCT) images of the cross-section of a cathode where (a) is the original image, (b) highlights the CL|MPL interface, (c) is a contrasted and manipulated image and (d) is the reconstructed three dimensional structure. Figure reprinted from Prass et al. [2] with permission from Elsevier.

The goal of this study is to investigate the effect of main crack characteristics identified in the previous subsection such as length, volume, area and tortuosity on the multi-phase transport dynamics.

Chapter 4

Modelling PEMFC cathodes

4.1 Overview

The focus of this thesis was to investigate the effect of crack and surface/interfacial protrusion using a combination of experimental characterization and numerical methods developed in the last few years at the University of Victoria's ESTP lab [4, 7, 62]. This chapter serves to introduce these methods and provide an overview of the theory to give context to the scope and limitations of the numerical techniques.

The first section describes briefly the two techniques used to generate numerical geometries of the catalyst layer for the computation. The geometries used in the numerical simulations involve a catalyst layer reconstructed from FIB-SEM imaging and are further manipulated to achieve higher resolution and obtain an ionomer and platinum distribution through stochastic measures.

The second section focuses on the lattice Boltzmann method, based on the work by Niu et al. [19], which allows simulation of two-phase flow in the porous layers. We begin with describing the lattice Boltzmann equation and the BGK approximation. The discretization is shown and the multiple relaxation time lattice Boltzmann method in 3 dimensions with

19 lattice velocities is presented. The governing equations based on the diffuse interface theory are introduced and their final form with the lattice Boltzmann method are presented and boundary conditions are discussed. The primary output of the method is a porous material sample with evolving water distribution at every time step.

The final section gives an overview on the pore scale model, the governing equations, the boundary conditions and the numerical method. The final geometry of the lattice Boltzman simulation with water distribution is used as input to the pore scale model.

The coupling between the numerical methods for the catalyst layer reconstruction, lattice Boltzmann method and the pore scale model is illustrated in figure 4.1. The geometry of the cathode is transferred between methods.

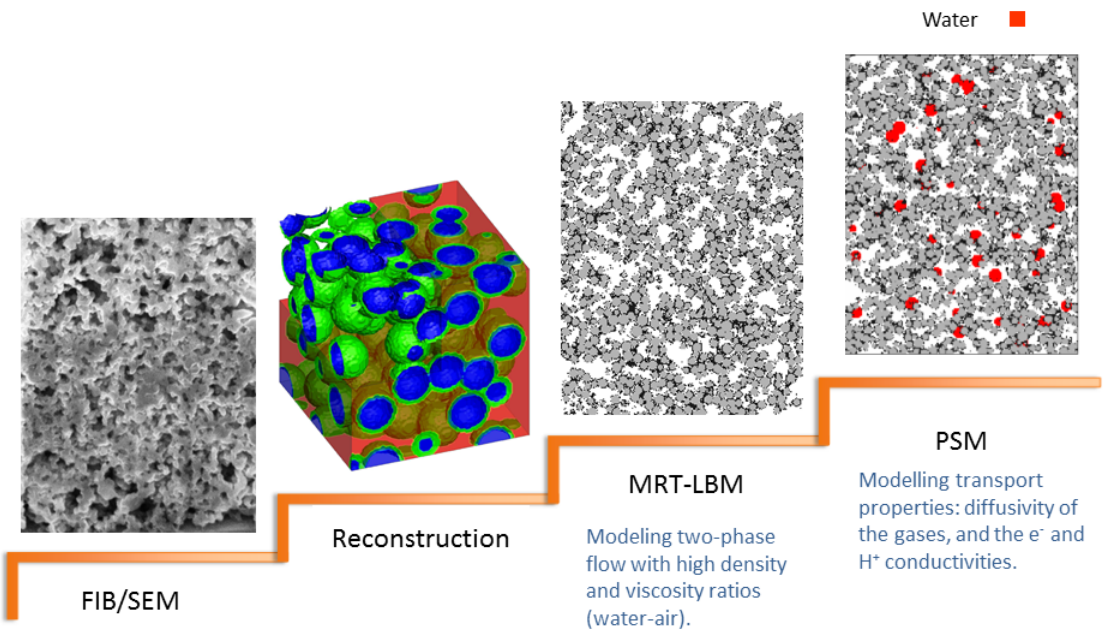

Figure 4.1: Coupling of the lattice Botlzmann technique and the pore scale model.

4.2 Catalyst layer reconstruction

The CL reconstruction procedure follows the previous work at UVic's ESTP lab and involves image acquisition, image processing, and numerical reconstruction of the sample. A brief description of the various steps is presented below with more details given in Singh et al. [62].

4.2.1 FIB-SEM reconstruction

The technique used to image and numerically reconstruct the catalyst layer relies first on Focused Ion Beam milling combined with Scanning Electron Microscopy (FIB-SEM). The physical catalyst layer sample is sliced using a sharp blade and a 3-D stack of images is obtained using a dual field-emission SEM and FIB where the electron beam is at an angle of 52 °with respect to the ion beam and the surface of the slice [63]. The slices were cut 20 nm apart and produced 50 slices and providing together a stack of images representing a three dimensional sample of size 1 μm × 1.98 μm × 1 μm.

The SEM images were processed by aligning the geometry to correct for the effects from the angled SEM image, and the solid and gas pixels were distinguished and contrasted to yield a binary image like the one in figure 4.2. The porosity was calculated to be 0.34 with an average pore size of 50 nm.

This geometry is used for lattice Boltzmann simulations since the method does not require differentiation between the carbon and ionomer since the simulation involves liquid water percolating through a solid, while disregarding the bulk properties of solid matrix of the porous structure.

Figure 4.2: One of the slices in the x-y plane of the catalyst layer of dimensions 1 μm × 1.98 μm × 1 μm. The white represents the gas and the grey represents the solid with no distinction between the carbon and ionomer.

4.2.2 Stochastic reconstruction

The catalyst layer consists of carbon black spheres with a thin ionomer coating and platinum particles. The pore scale model simulates mass transport, charge transport, and electrochemical reactions, therefore a geometry which distinguishes between the ionomer, platinum, and carbon solids is required [7].

To produce a high resolution geometry of this kind, an initial seed of carbon spheres was optimized to match with the FIB-SEM images of lower resolution using a two point correlation function. The generated image has an isotropic resolution of 5.95 nm compared to the originally imaged CL which is limited to a resolution of 20nm in one direction [62]. The geometry is generated with a prescribed mean and standard deviation for the carbon sphere radius, porosity, ionomer to carbon ratio as well as platinum particle size and loading.

To numerically represent the presence of the ionomer, the cells which are next to a carbon cell are considered for conversion from gas to ionomer. The platinum particles are considered as non-volumetric elements and placed at the surface between carbon spheres and ionomer.

This method was used to generate the reconstructed catalyst layer displayed in figure

4.3 and the three dimensional reconstruction is displayed in figure 4.4.

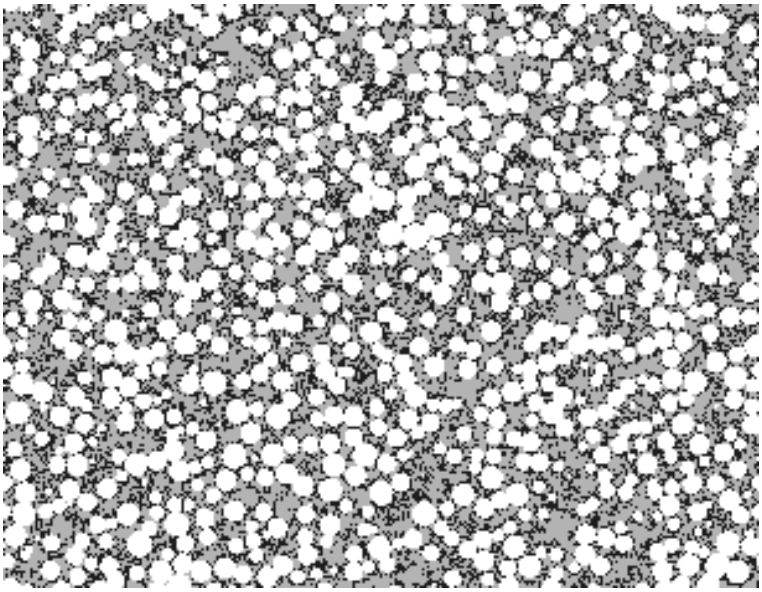

Figure 4.3: One of the slices in the x-y plane of the catalyst layer of dimensions 1.398 μm × 1.815 μm × 1.499 μm. The white represents the carbon, the black represents the ionomer and the grey represents the gas.

4.3 Lattice Boltzmann method (LBM)

4.3.1 Boltzmann equation

The Boltzmann equation, which represents the velocity distribution function of particles, is at the foundation of the LBM. To describe the arrangement of particles in a macroscopic system, Ludwig Boltzmann applied probability theory to microscopic properties.

In the context of a single phase gas, we can describe the probability, p, of a particle with a distribution function $f(\mathbf{r})$ in the gas to be located in a volume, $d\mathbf{r}$, is defined as follows:

$$p(\mathbf{r} \in V) = \int_V f(\mathbf{r}) dx dy dz = \int_V f(\mathbf{r}) d\mathbf{r}. \tag{4.1}$$

The macroscopic properties of interest such as velocity, pressure, density can readily be

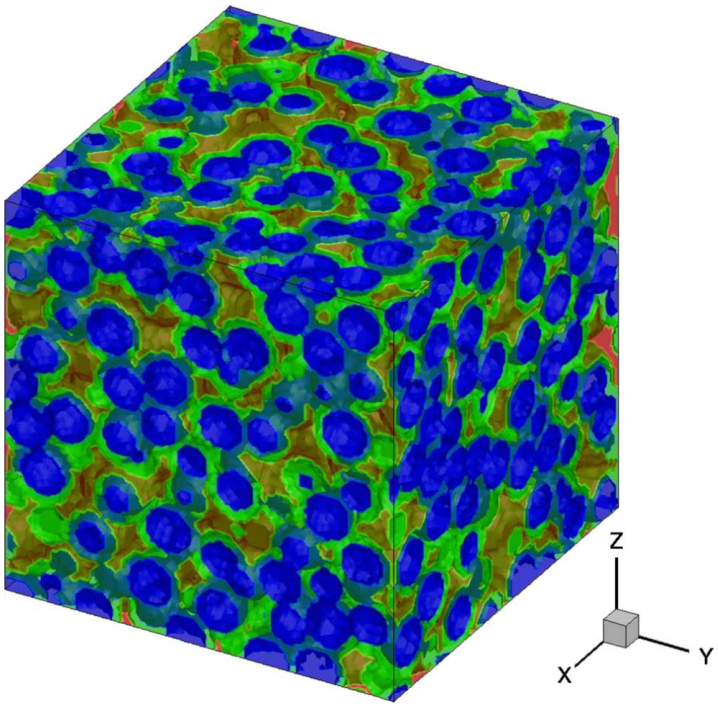

Figure 4.4: A reconstructed catalyst layer of dimensions 200 nm $\times$ 200 nm $\times$ 200 nm. The carbon spheres are in blue, the ionomer in green, and the gas pores in yellow. Figure from Lange et al. [3].

obtained from the velocity distribution function, $\mathbf{u} = (u, v, w)$. Combining the spacial and velocity distribution functions, p, is the probability of a particle to have a velocity which exists in the velocity space $d\mathbf{u}$ as well as having spacial coordinates within the volume $d\mathbf{r}$.

$$p(\mathbf{u},\mathbf{r}) = \int f(\mathbf{u},\mathbf{r}) d\mathbf{u} d\mathbf{r} \tag{4.2}$$

To obtain the distribution function for the subset of m particles in a system of N particles, we integrate out all particles outside of the subset of interest by integrating over infinite coordinate space which sets all probabilities in this limit to 1. The distribution function for m, and two particles are expressed in equation 4.3 and 4.4 [64].

$$f^m(\mathbf{u}_1, \mathbf{r}_1, ..., \mathbf{u}_m, \mathbf{r}_m) = \int_{-\infty}^{\infty} f^N(\mathbf{u},\mathbf{r}) d\mathbf{u}_{m+1} d\mathbf{r}_{m+1} ... d\mathbf{u}_N d\mathbf{r}_N \tag{4.3}$$

$$f^1(\mathbf{u}_1, \mathbf{r}_1) f^2(\mathbf{u}_2, \mathbf{r}_2) = f^2(\mathbf{u}_1, \mathbf{r}_1, \mathbf{u}_2, \mathbf{r}_2) = \int_{-\infty}^{\infty} f^N(\mathbf{u},\mathbf{r}) d\mathbf{u}_3 d\mathbf{r}_3 ... d\mathbf{u}_N d\mathbf{r}_N \tag{4.4}$$

These equations exhibit the principle of molecular chaos as the colliding particles have uncorrelated velocities which are independent of position. The Boltzmann equation presented in equation A.11 is obtained by considering molecular fluxes and collisions in a representative space as detailed in Appendix A.

$$\frac{\partial}{\partial t}(nf) + \mathbf{u} \cdot \frac{\partial}{\partial \mathbf{r}}(nf) + \frac{\mathbf{F}}{m} \cdot \frac{\partial}{\partial \mathbf{u}}(nf) = \int_{-\infty}^{\infty} \int_{0}^{4\pi} n^2 (f' f_1' - f f_1) \mathbf{u}_r (\sigma d\Omega) d\mathbf{u}_1. \tag{4.5}$$

We tagged n along for conceptual purposes in equation A.1, but we can drop it to have an expression with only the probability density function f. The following form is common, where $Q_f(f, f)$ is the collision integral [65].

$$\partial_t f + \mathbf{u} \partial_{\mathbf{r}} f + \frac{\mathbf{F}}{m} \partial_{\mathbf{u}} f = Q_f(f, f). \tag{4.6}$$

$$Q_f(f, f) = \int \int (f' f_1' - f f_1) \mathbf{u}_r \sigma d\Omega d\mathbf{u}_1. \tag{4.7}$$

The BGK approximation

The Bhatnagar-Gross-Krook (BGK) collision model introduces a relaxation term to simplify the collision integral, $Q_f(f, f)$ [66].

The distribution function, f, can be considered as having an equilibrium, $f^{(eq)}$, and non-equilibrium, $f^{(neq)}$, component.

$$f = f^{(eq)} + f^{(neq)} \tag{4.8}$$

The model assumes that the mean free path of the particles is much smaller that the

characteristic length scale of the system, such that $Kn \ll 1$. In this case, we can approximate that the distribution function at equilibrium, $f^{(eq)}$, follows the Maxwell distribution function for a monoatomic gas, as follows [65].

$$f^{(eq)} = n \left(\frac{m}{2\pi k_B T} \right)^{\frac{3}{2}} e^{-\frac{m}{2k_B T}(\mathbf{u}-\bar{\mathbf{u}})^2}, \tag{4.9}$$

where k_B is the Boltzmann constant.

The distribution function for the perturbation of equilibrium, $f^{(neq)}$, can be approximated to be the first Chapman Enskog expansion of the distribution function, f.

The simpler term, $Q_f(f)$, can be conceptualized by considering that every collision changes the distribution function proportionally to the departure from equilibrium, where τ is the collision time. The long form expression, equation 4.11, is used for computational purposes.

$$Q_f(f) = -\frac{1}{\tau} f^{(neq)}, \tag{4.10}$$

$$Q_f(f) = -\frac{1}{\tau}(f - f^{(eq)}), \tag{4.11}$$

The BGK form, also referred to as "single time relaxation", of the Boltzmann equation is thus,

$$\partial_t f_i + \mathbf{u}\partial_{\mathbf{r}} f + \frac{\mathbf{F}}{m}\partial_{\mathbf{u}} f = -\frac{1}{\tau}(f - f^{(eq)}). \tag{4.12}$$

The mass density, ρ, can be extracted as follows.

$$\rho(\mathbf{r}, t) = \int m f(\mathbf{r}, \mathbf{u}, t) d\mathbf{u} \tag{4.13}$$

4.3.2 Lattice Boltzmann equation

The lattice Boltzmann equation is a discretized form of the Boltzmann equation. The distribution function $f(\mathbf{r}, \mathbf{u}, t)$ is reduced to a discrete distribution function in physical space and time, $f_i(\mathbf{r}, t)$, and the velocity space is discretized such that each discrete distribution function have an associated discrete velocity, $\mathbf{e}_i$. The discretization is shown below.

$$\frac{\partial f_i}{\partial t} + \mathbf{e}_i \frac{\partial f_i}{\partial \mathbf{r}} + \mathbf{a} \frac{\partial f_i}{\partial \mathbf{e}_i} = -\frac{1}{\tau}(f_i - f_i^{(eq)}) \tag{4.14}$$

We can expand and substitute $\mathbf{e}_i = \Delta\mathbf{r}/\Delta t$ to obtain the BGK lattice Boltzmann equation expressed in equation 4.17.

$$\frac{f_i(\mathbf{r}, t + \Delta t) - f_i(\mathbf{r}, t)}{\Delta t} + \mathbf{e}_i \frac{f_i(\mathbf{r} + \Delta\mathbf{r}, t + \Delta t) - f_i(\mathbf{r}, t + \Delta t)}{\Delta r} = -\frac{1}{\tau}(f_i - f_i^{(eq)}) - \mathbf{a}\nabla_{\mathbf{e}} f_i \tag{4.15}$$

$$\frac{f_i(\mathbf{r}, t + \Delta t) - f_i(\mathbf{r}, t)}{\Delta t} + \frac{f_i(\mathbf{r} + \mathbf{e}_i\Delta t, t + \Delta t) - f_i(\mathbf{r}, t + \Delta t)}{\Delta t} = -\frac{1}{\tau}(f_i - f_i^{(eq)}) - \mathbf{a}\nabla_{\mathbf{e}} f_i \tag{4.16}$$

$$f_i(\mathbf{r} + \mathbf{e}_i\Delta t, t + \Delta t) - f_i(\mathbf{r}, t) = -\frac{\Delta t}{\tau}(f_i - f_i^{(eq)}) - \mathbf{a}\nabla_{\mathbf{e}} f_i \Delta t \tag{4.17}$$

The terms on the left hand side represent the streaming process where particles scatter after the collision and flow in the system. The term on the right and side embodies the processes involved in the collision of particles.

The BGK collision model alone leads to numerical instabilities and a viscosity-dependent velocity field [67]. A multiple relaxation time (MRT) lattice Boltzmann technique adjusted for two-phase flows with high density ratios using two distribution functions mitigates these issues. The method and its implementation are presented in the following section.

4.3.3 Multiple relaxation time lattice Boltzmann method (MRT-LBM)

Diffuse interface theory

The diffuse interface theory allows us to model multi-phase flows with high density ratios and various viscosities [19, 68, 69]. The behaviour of the fluid is governed by the Navier-Stokes equation expressed in equation 4.18, and the Cahn-Hilliard equation expressed in equation 4.19, allows one to model the interface between the liquid and gas phases.

$$\frac{\partial \rho \mathbf{u}}{\partial t} + \nabla \cdot \rho \mathbf{u}\mathbf{u} = -\nabla \cdot \mathbf{P} + \eta \nabla^2 \mathbf{u} + \mathbf{F}_b \tag{4.18}$$

$$\frac{\partial \varphi}{\partial t} + \nabla \cdot \varphi \mathbf{u} = M \nabla^2 \mu \tag{4.19}$$

Where $\mathbf{u}$ is the fluid velocity, ρ is the mass density, η is the viscosity, $\mathbf{P}$ is the gradient of the pressure tensor, $\mathbf{F}_b$ is the body force, φ is the density difference between two phases, M is the mobility, and μ is the chemical potential.

The MRT-LBM technique is applied using both the Navier-Stokes equation where the distribution function is of the velocity field with a total density of different phases and the Cahn-Hilliard equation where the distribution function is the local order parameter φ, which allows for tracking of the interface [19].

D3Q19 model

The numerical solution of the LB equation requires discretization in a lattice domain. The D3Q19 model was proposed by d'Humières et al. [70] is used which has 19 lattice velocities in a cubic lattice. The 3D lattice is shown in figure 4.5 and the particle can stream in one of 19 directions, including remaining in its position. The model is defined by

the following lattice velocities, where i represents the different directions:

$$e_i = \begin{cases} (0,0,0) & i = 0 \\ (\pm 1,0,0),(0,\pm 1,0),(0,0,\pm 1) & i = 1-6 \\ (\pm 1,\pm 1,0),(\pm 1,0,\pm 1),(0,\pm 1,1) & i = 7-18 \end{cases} \tag{4.20}$$

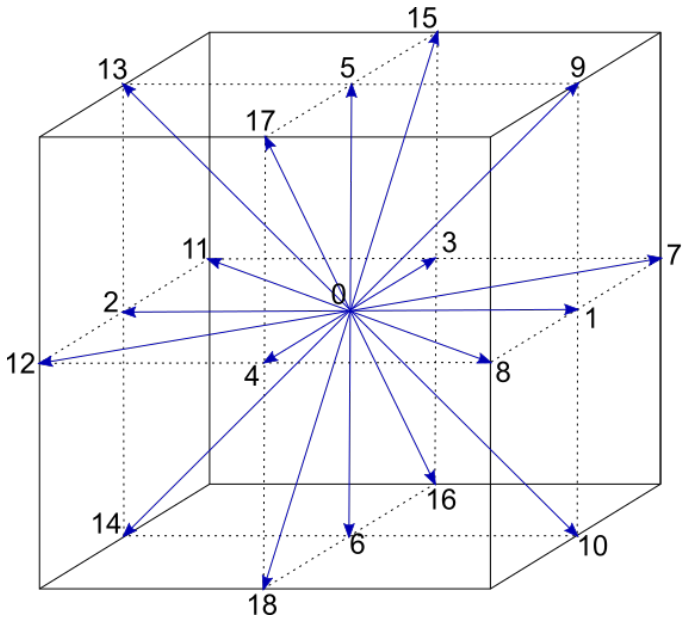

Figure 4.5: 3D lattice for the D9Q19 model .

The lattice tensors of high rank are not always isotropic due to the symmetry of the lattices, but this can be corrected by adding weighing coefficients w_i for the different speeds corresponding to different directions. The adjusted equilibrium distribution function, $f^{(eq)}$, weighing coefficients are indicated in equation 4.21 and 4.22 where $c = \delta\mathbf{r}/\delta t$ is the ratio between the lattice spacing $\delta\mathbf{r}$ and the time step δt, both set to 1.

$$f_i^{(eq)} = -w_i\rho\left[1 + \frac{\mathbf{e}_i \cdot \mathbf{u}}{c^2} + \frac{(\mathbf{e}_i \cdot \mathbf{u})^2}{2c^4} - \frac{|\mathbf{u}|^2}{2c^2}\right] \tag{4.21}$$

$$w_i = \begin{cases} \frac{1}{3} & i = 0 \\ \frac{1}{18} & i = 1 - 6 \\ \frac{1}{36} & i = 7 - 18 \end{cases} \tag{4.22}$$

The local density, ρ and the momentum, **j**, can be calculated.

$$\rho = \sum_i f_i \tag{4.23}$$

$$\mathbf{j} = \rho\mathbf{u} = \sum_i e_i f_i \tag{4.24}$$

The transformation matrix, **M**, is used to convert the distribution functions f_i and $f_i^{(eq)}$ in velocity space to macroscopic variables such that

$$\mathbf{m} = \mathbf{Mf} = (\rho, e, j_x, q_x, j_y, q_y, j_z, q_z, 3p_{xx}, p_{ww}, p_{xy}, p_{yz}, p_{xz}, t_{xyz})' \tag{4.25}$$

where **m** is the velocity moment, ρ is density, e is the energy, j is momentum, q is related to the energy flux, p is pressure.

A relaxation matrix, $\mathbf{\Lambda}$, has diagonal elements which are the relaxation parameters corresponding to each moment in **m**.

Following the diffuse interface theory, the lattice Boltzmann technique is applied using the Navier-Stokes and Cahn-Hilliard equations and yields two distribution functions. The final discretized form with the multiple relaxation time adjustment is expressed by the density distribution function vector, **f**, in equation 4.26 and the order-parameter distribution function vector, **g**, in equation 4.27.

$$\mathbf{f}(\mathbf{r}+\mathbf{e}_i\delta t, t+\delta t) = \mathbf{f}(\mathbf{r},t) - \mathbf{M}^{-1}\mathbf{\Lambda}_f \left(\mathbf{m}_f(\mathbf{r},t) - \mathbf{m}_f^{eq}(\mathbf{r},t)\right) + \delta t \left(\mathbf{I} - \frac{1}{2}\mathbf{M}^{-1}\mathbf{\Lambda}_f\mathbf{M}\right)\mathbf{G}(\mathbf{r},t) \tag{4.26}$$

$$\mathbf{g}(\mathbf{r} + \mathbf{e}_i\delta t, t + \delta t) = \mathbf{g}(\mathbf{r},t) - \mathbf{M}^{-1}\mathbf{\Lambda}_g(\mathbf{m}_g(\mathbf{r},t) - \mathbf{m}_g^{eq}(\mathbf{r},t)) \tag{4.27}$$

where the final term is a result of the Taylor expansion of the force term in equation 4.17, and **G** is defined in equation 4.28.

$$\mathbf{G}(\mathbf{r},t) = w_i \frac{\mathbf{e}_i - \mathbf{u}}{c^2} \cdot (\mathbf{F}_{ext} + \mu\nabla\phi) \tag{4.28}$$

The density distribution vector, **f**, and the order parameter vector, **g**, describe the dynamic behaviour of the multiphase system and are solved for each location and time step.

4.3.4 Boundary conditions

In this numerical technique, a fixed volume of liquid water is placed at the boundary associated with the high pressure, the lower boundary perpendicular to the y axis. The opposite boundary is assigned a lower pressure in the y direction. The simulation then allows water to drain through the pores of the closed volume towards the boundary with the lowest pressure. A contact angle, θ, is also prescribed to the system.

Periodic boundary condition

As illustrated in figure 4.6, periodic boundary conditions are implemented for the boundaries perpendicular to the x and z axes. If the fluid reaches a periodic boundary, it will leave the system at this edge and emerge from the opposite boundary into the system with the

same properties such as direction and velocity.

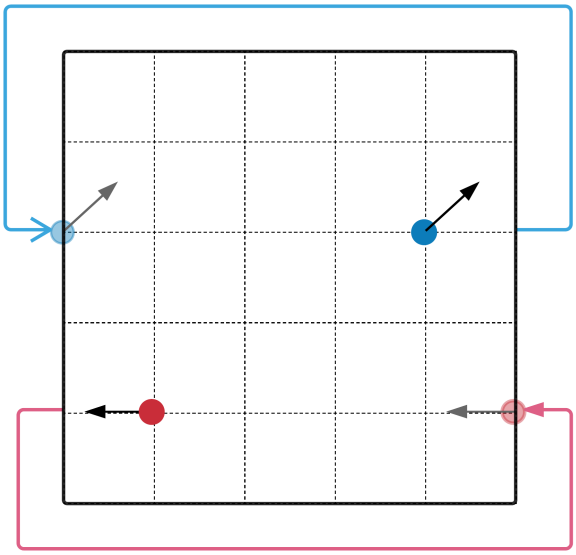

Figure 4.6: Schematic demonstrating the periodic boundary condition.

Bounce-back boundary condition

In the case where a fluid encounters a solid such as a carbon particle, the bounce-back condition is applied to satisfy the no-slip condition for continuum flow where the fluid has a zero velocity at the boundary. As illustrated in figure 4.7, properties of a particle colliding with a solid particle are reflected by 180 degrees.

4.4 Pore scale model

4.4.1 Governing equations

The model consists of governing equations for mass transport and electrochemical reactions. Oxygen transport is driven by diffusion while water vapour transport has an electro-osmotic drag component in addition to diffusion. The diffusion component of the gases

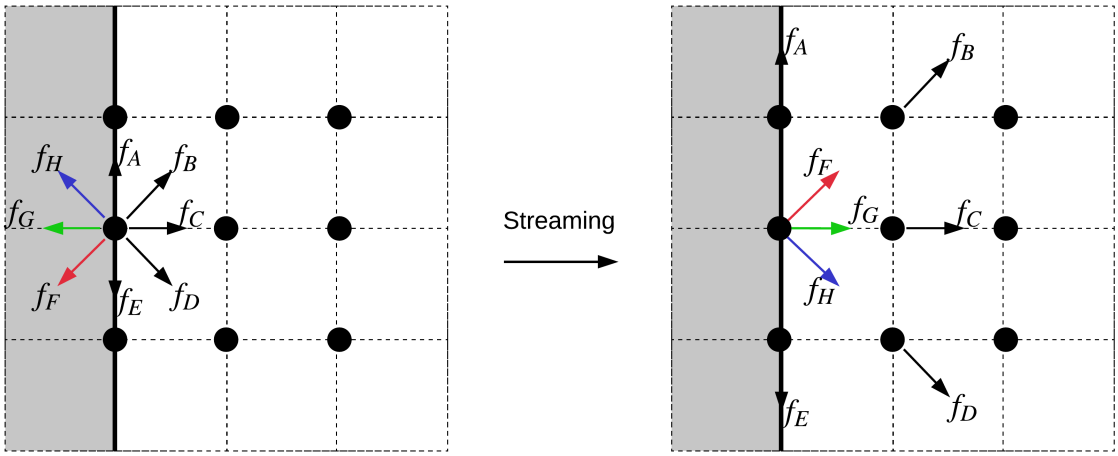

Figure 4.7: Schematic demonstrating the bounce back boundary condition.

is expressed with Frick's law. The proton and electron transport parameters are calculated using Ohm's law. The following expression represents the transport flux vector including oxygen, water vapour, proton and electron transport fluxes [3].

$$\mathbf{\Gamma_t} = \begin{bmatrix} \Gamma_{O_2,t} \\ \Gamma_{H_2O,t} \\ \Gamma_{H^+,t} \\ \Gamma_{e,t} \end{bmatrix} = \begin{bmatrix} -D_{O_2}\nabla C_{O_2} \\ -D_{H_2O}\nabla C_{H_2O} - \frac{n_d\sigma_m}{F}\nabla\phi_m \\ -\sigma_m\nabla\phi_m \\ \sigma_s\nabla\phi_s \end{bmatrix} \tag{4.29}$$

$\mathbf{\Gamma_t}$ is the transport flux, D_{O_2} and D_{H_2O} are the oxygen and water vapour diffusivities, C_{O_2} and C_{H_2O} are the oxygen and water vapour concentrations, ϕ_m and ϕ_s are the membrane potential (proton transport) and solid potential (electron transport) respectively, σ_m and σ_s are the membrane and solid conductivities. F is the Faraday constant and n_d is the electro-osmotic drag coefficient.

A reaction flux vector, $\mathbf{\Gamma_r}$, is calculated for each parameter using the Tafel equation from electrochemical kinetics theory, which relates the rate of an electrochemical reaction to the overpotential [3]. The reaction flux vector is expressed as follows.

$$\mathbf{\Gamma_t} = \begin{bmatrix} \Gamma_{O_2,r} \\ \Gamma_{H_2O,r} \\ \Gamma_{H^+,r} \\ \Gamma_{e,r} \end{bmatrix} = \begin{bmatrix} \frac{1}{4F} i_0 \frac{C_{O_2}}{C_{O_2,ref}} e^{-\frac{\alpha_c F}{RT}(\phi_s - \phi_m)} \\ -\frac{1}{2F} i_0 \frac{C_{O_2}}{C_{O_2,ref}} e^{-\frac{\alpha_c F}{RT}(\phi_s - \phi_m)} \\ i_0 \frac{C_{O_2}}{C_{O_2,ref}} e^{-\frac{\alpha_c F}{RT}(\phi_s - \phi_m)} \\ i_0 \frac{C_{O_2}}{C_{O_2,ref}} e^{-\frac{\alpha_c F}{RT}(\phi_s - \phi_m)} \end{bmatrix} \tag{4.30}$$

$\mathbf{\Gamma_r}$ is the reaction flux, i_0 is the exchange current density, α_c is the charge transfer coefficient, $C_{O_2,ref}$ is the reference oxygen concentration at environmental conditions, R is the universal gas constant and T is the temperature. The values of the reference parameters used in this model are defined in Lange et al. (2010) [3].

The system is assumed to be steady-state and isothermal, and combining the fluxes, transport for each species is governed by.

$$\nabla \cdot (\mathbf{\Gamma_t} + \mathbf{\Gamma_r}) = \nabla \cdot (\mathbf{\Gamma}) = \mathbf{0} \tag{4.31}$$

Diffusion in the pores

The oxygen and water vapour diffusivity, D_{O_2} and D_{H_2O} are obtained by considering both the bulk diffusivity, D_b, and Knudsen diffusicity, D_{Kn} and are described by the following relation [71].

$$\frac{1}{D_{H_2O}} = \frac{1}{D_{Kn,H_2O}} + \frac{1}{D_{b,H_2O}} \tag{4.32}$$

$$\frac{1}{D_{O_2}} = \frac{1}{D_{Kn,O_2}} + \frac{1}{D_{b,O_2}} \tag{4.33}$$

The bulk oxygen diffusivity for each gas is assigned a constant value representing the binary diffusion, diffusion between two molecules, of the gas into nitrogen [7].

Knudsen diffusion is accounted for when the mean free path of the particle is of the same order as the pore size. Under these conditions, the particles frequently collide with the

boundaries. This is the case for gasses in a small capillary pore such as the one illustrated in figure 4.8 since low density fluids have a large mean free path. The Knudsen diffusivity is calculated as follows, using the kinetic theory of gases and the dusty gas model [72].

$$D_{Kn} = \frac{\langle d \rangle \langle v \rangle}{3} = 4850 \langle d \rangle \sqrt{\frac{T}{M}} \tag{4.34}$$

d is the diameter of the pore, v is the mean molecular velocity and M is the molecular weight of the gas.

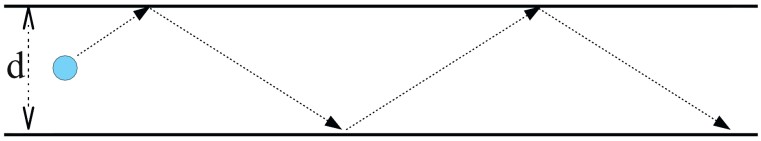

Figure 4.8: Schematic of a molecule undergoing Knudsen diffusion in a capillary. Figure from Lange et al. 2012 [4].

The total diffusivity is predominantly represented by the bulk diffusivity in relatively large pores, and the Knudsen diffusivity in small pores [4] . Numerically, Knudsen diffusivity depends on the calculated value of the pore diameter. Solving for this value is a challenge due to the random three dimensional shape of the pores.

4.4.2 Boundary conditions

Dirichlet boundary conditions are applied to the two parallel faces along the y-axis, where the concentration of the gases, the potentials, and the temperature are different at each boundary. Their values are displayed in table 4.1 [4]. Periodic boundary conditions are used for the remaining four faces. These conditions drive the average mass transport in the z-direction. The system is set to operate at a relative humidity of 98%, so liquid water is not generated. However, liquid water can be present in the system, although it is static and phase interactions are not modelled.

Table 4.1: Boundary conditions for the parallel surfaces along the y-direction.

Variable	Boundary 1	Boundary 2
C_{O_2}	$10.1 \times 10^{-6} \frac{mol}{cm^3}$	$10.0 \times 10^{-6} \frac{mol}{cm^3}$
C_{H_2O}	$15.9 \times 10^{-6} \frac{mol}{cm^3}$	$16.0 \times 10^{-6} \frac{mol}{cm^3}$
ϕ_m	1.7 V	1.708 V
ϕ_s	1.3 V	1.30018 V
T	353.0 K	353.1 K

4.4.3 Numerical method

The governing equations are discretized in mesh elements using the finite volume method [7]. To solve for the fluxes, the system expressed by equation 4.31 is integrated over a control volume and by using Green's theorem, is converted to a surface integral as follows.

$$\iiint \nabla \cdot (\mathbf{\Gamma}) \mathbf{dV} = \iint \mathbf{\Gamma} \cdot \mathbf{AdS} \approx \sum \mathbf{\Gamma} \cdot \mathbf{A} = \mathbf{0} \tag{4.35}$$

Without the consideration of electrochemical reactions, the influx of a mass type such as an electron, proton, oxygen or water molecule in a computational cell would be equal to its outflux. Lange et al. [7] showed that when the electrochemical reactions were considered for the calculation of the fluxes, the difference in the influx and outflux was small. The outflux value is therefore used as an approximation for the flux when computing the transport parameters.

By Fourrier and Frick's law, the flux of a quantity, x, can also be expressed as

$$\Phi_x = -X_{eff} \frac{(x_2 - x_1)}{l}, \tag{4.36}$$

where l is the length of the solution domain, X_{eff} is the effective transport parameter and x_1 and x_2 are the values of the quantity at the boundaries. Using equation 4.36 and fluxes

obtained from equation 4.35, the effective transport properties are computed.

In order to calculate Knudsen diffusivity, an effective pore diameter is calculated for each computational cell tagged as a gas. This is achieved by averaging thirteen diameters obtained in different directions: along the x, y and z axis, two diagonals for each of the x-y, x-z, and y-z planes with a slope of one and negative one, and four diagonal directions through the three dimensional space [73].

The system is solved using an inexact Newton method, and the simulations are considered to have converged when the nonlinear root mean square calculated with a Newton-Raphson solver converges to machine zero [7]. The simulation is parallelized to run on 64 processors, using a localized ILU preconditioner [3].

Chapter 5

Modelling transport properties in perforated cathode CL and MPL

5.1 Overview

The effect of select crack characteristics such as size of aperture, degree of protrusion and tortuosity on liquid water, oxygen transport and conductivity are studied using the MRT-LBM and PSM models described in the previous chapter. The parameters and initial conditions are described for these models and results are discussed.

5.2 Drainage process in the cathode

The water is generated in the catalyst layer of the cathode at electrochemically active sites, then a portion of it moves towards the gas diffusion layer while an other moves towards the membrane if the pressure is insufficient to drive the water through the MPL, and/or if water is taken up by the membrane. The modelling approach used here resolves water transport at the pore scale and necessitates some simplifications, including decoupling from the adjacent boundaries (membrane and channel). The computationally inten-

sive LBM simulations also do not account for internal water production which requires coupling to the electrochemical reaction. Water transport in porous layers is modelling the drainage process, meaning that water supply is prescribed at one of the boundaries and the acting forces from capillary action and a pressure gradient will encourage the water to percolate through the layer. This method is effective to determine preferential pathways for liquid water due to unobstructed capillary action in a dry sample, it also represents the simulation analogue to physical imbibition/drainage experiments commonly used to characterize porous media.

It is to be noted that after the water travels across the layer and reaches the end of the computational domain, the water is not removed and continues to accumulate, increasing liquid saturation. In real cathodes, when water reaches the interface, referred to as breakthrough, the water is removed from the MPL into the GDL. The breakthrough point is made evident and discussed for the experiments.

Several geometries and corresponding dimensions are used in this study, so the pressure gradient across the boundaries perpendicular to the flow direction (y) for all experiments is 1.8kPa per number of lattice units in the y direction. Since the lattice unit is 20nm for these experiments, the pressure gradient is 90Pa/nm. The number of iterations performed was 100 000, which represents time steps in LB units. In this work the lattice length scale, δr, and lattice time step, δt, are unity such that $\delta r = \delta t = \delta = 1$.

The contact angle, which is the angle formed by the liquid interface on a solid, describes the wettability. The contact angle of the system was set as constant throughout the system and a value of 110° was used based on reported values for common hydrophobic (nonwettable) materials in the cathode [74].

Other constants include surface tension, which was set to 0.0625 N/m, and the initial density of liquid and gas which were chosen to be 1000 kg/m^3 and 1.14 kg/m^3 respectively.

5.2.1 Perforated reconstructed catalyst layers

An initial study is performed on a reconstructed catalyst layer from FIB/SEM imaging as described in section 4.2.1 and has dimensions 1 μm × 1.98 μm × 1 μm. This simulation focuses on liquid water transport so the geometry does not need to distinguish between ionomer and platinum and is therefore composed of only two phases: solid and gas. Various geometries with different crack structures were constructed by replacing predetermined solid cells with gas cells. Two notable sets of experiments were conducted with the reconstructed catalyst layer.

The first set of structures were constructed to study the effect of the length of cracks in the porous layer. As shown in figure 5.3, the crack stems from the bottom of the CL, the boundary connected to a large volume of water, and the base area of 14400 nm^2 is constant as the length of the crack is varied. The water transport for a geometry with no cracks, a crack length of 0.5μm, and a crack spanning the length of the CL can be visualized in figure 5.1. In the second experiments the area of the crack is varied for a constant length of crack, which is 1.98 μm and spans the length of the CL. The evolution of saturation in the domain with time is shown for both experiments in figure 5.2.

These simulations suggest that the saturation increases proportionally to the area of the crack, and that the elongated crack reaches breakthrough more rapidly. The simulations also suggests that the short interfacial crack have very little effect on water transport.

Due the limitations of computational resources, the computational domain is too small to represent some of the large cracks discussed in section 3.4, so small cracks are considered. A drawback of small cracks is that they can be of similar size to large pores. For example, in the cracked reconstructed geometry, large pores are connected to the perforation as observed in figure 5.3. Large pores can also encourage water transport which can make it difficult to isolate the effect of the crack on transport. In fact, some of the larger pores are located at the lower boundary and can ambiguate our study of interfacial cracks.

These results corroborate the two dimensional lattice Boltzmann study by Han and Meng [18], where it was observed that cracks give a preferential path for liquid water transport due to their lower capillary pressure with respect to their surroundings. Performing the analysis with a three dimensional model is important since the effect of friction can not be fully captured due to a smaller surface area in two dimensions. Information on porosity and surface area can not both be representative of a realistic geometry in a two dimensional modelling scheme.

(a) No perforation, $t = 7000\ \delta$

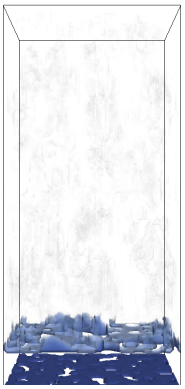

(b) 0.5µm perforation, $t = 7000\ \delta$

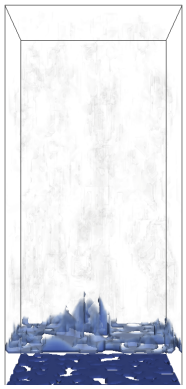

(c) 1.5µm perforation, $t = 7000\ \delta$

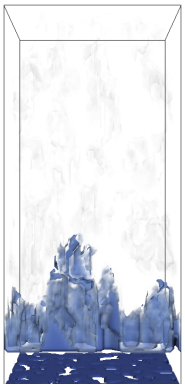

(d) No perforation, $t = 20000\ \delta$

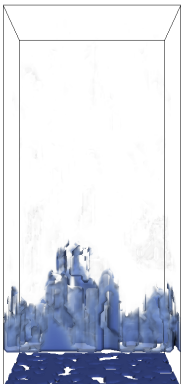

(e) 0.5µm perforation, $t = 20000\ \delta$

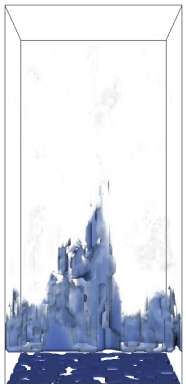

(f) 1.5µm perforation, $t = 20000\ \delta$

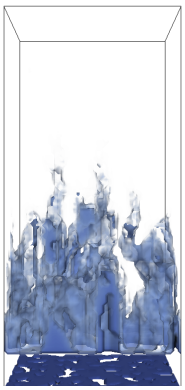

(g) No perforation, $t = 50000\ \delta$

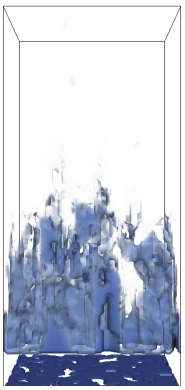

(h) 0.5µm perforation, $t = 50000\ \delta$

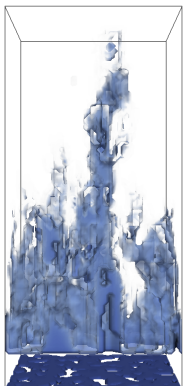

(i) 1.5µm perforation, $t = 50000\ \delta$

Figure 5.1: Water transport through a reconstructed catalyst layer of dimensions 1 µm × 1.98 µm × 1 µm. The base area of the perforation is constant and the depth of the crack is indicated under each image.

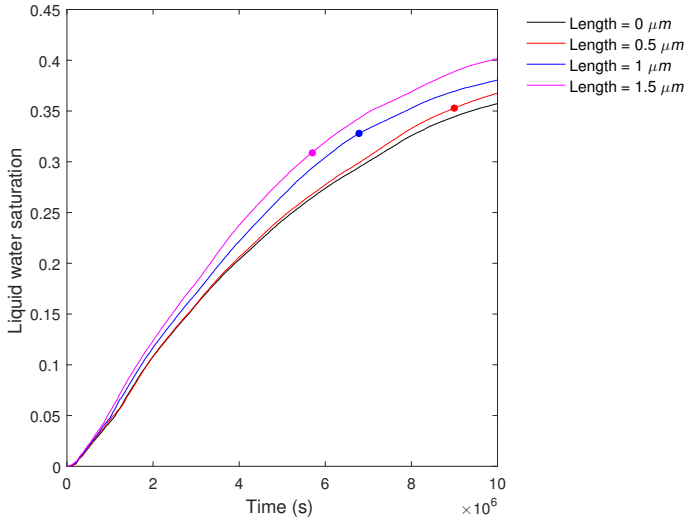

(a) Evolution of saturation for varying lengths of cracks and constant base area.

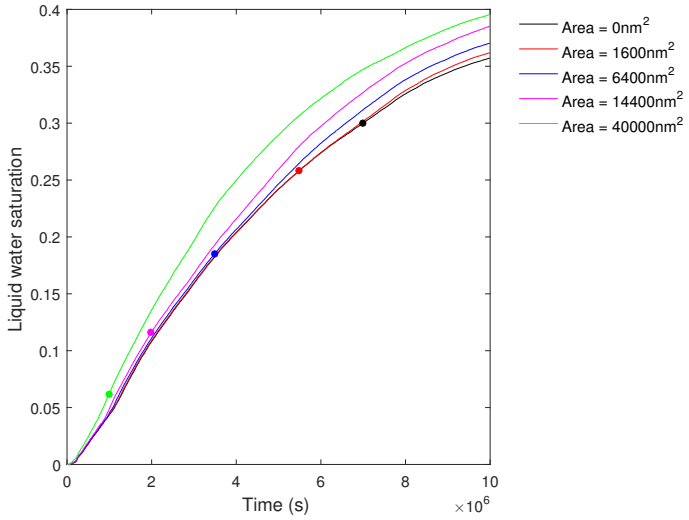

(b) Evolution of saturation for varying base area of cracks and a constant length which spans the CL.

Figure 5.2: Evolution of saturation in the CL for different crack structures. The markers indicate the breakthrough points for each geometry.

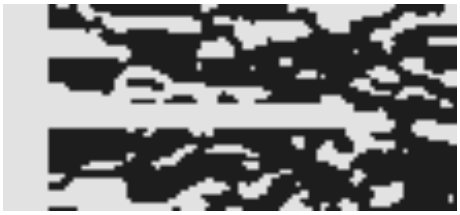

Figure 5.3: Slice of the reconstructed geometry with a perforation 1.5μm in length along the y axis.

5.2.2 Perforated idealized catalyst layers

The irregular pore structure of the reconstructed catalyst layer poses difficulties when studying the effect of other cracks in the porous media. As we have a reasonably good understanding of liquid water transport in non cracked porous media from the literature, the effect of cracks should be isolated.

An idealized porous structure consisting of regularly positioned spheres is therefore proposed for the catalyst layer which represents the salient characteristic of the layer. A porosity of 0.40 was achieved compared to 0.34 for the reconstructed layer used in the first experiment, however it is still representative of the porosities observed in catalyst layers [75]. The size of the spheres, $r = 100$nm are larger than the carbon particles used in the manufacturing process, as they are meant to represent not only the carbon, but also the large grouping of agglomerated carbon spheres with ionomer in the catalyst layer.

The spheres were arranged in a hexagonal close-packed (hcp) symmetry since staggering the spheres avoids the tubular gaps present in some symmetric lattice structures such as the simple cubic lattice. A slice of the idealized geometry is presented in figure 5.4.

Figure 5.4: Slice of the idealized CL of dimensions 1 μm × 1.98 μm × 1 μm with no perforations. The solid and gas are represented by white and black respectively.

The first set of experiment, where the base area of the cracks remained constant as the length increased was reproduced using this new geometry and the results can be visualized in figure 5.5. Compared to the reconstructed geometry, the new geometry shows a similar rate of water transport for all cracked and non cracked structures, however the effect from the crack is accentuated and isolated from other capillary effects in the porous structure.

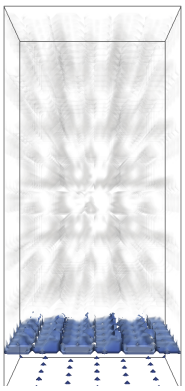

(a) No perforation, $t = 7000\ \delta$

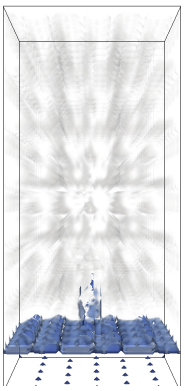

(b) 0.5µm perforation, $t = 7000\ \delta$

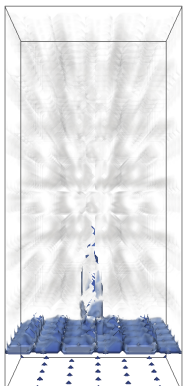

(c) 1.5µm perforation, $t = 7000\ \delta$

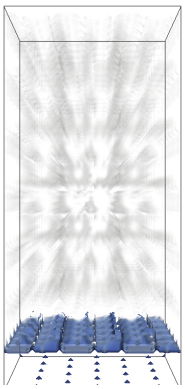

(d) No perforation, $t = 20000\ \delta$

(e) 0.5µm perforation, $t = 20000\ \delta$

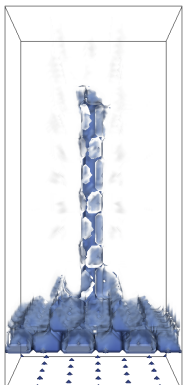

(f) 1.5µm perforation, $t = 20000\ \delta$

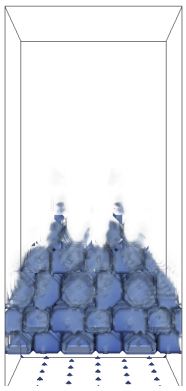

(g) No perforation, $t = 50000\ \delta$

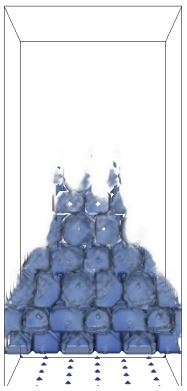

(h) 0.5µm perforation, $t = 50000\ \delta$

(i) 1.5µm perforation, $t = 50000\ \delta$

Figure 5.5: Water transport through a symmetrically constructed catalyst layer of dimensions 1 µm × 1.98 µm × 1 µm. The base area of the crack is constant and the depth of the crack is indicated under each image.

5.2.3 Effect of crack morphology on liquid water transport

Using the idealized porous structure introduced in the previous section to isolate the effect from the crack, select characteristics of cracks such as crack depth for a fixed aperture size, degree of protrusion and tortuosity are explored for cracks in the CL and MPL. A hexagonal close-packed (hcp) symmetry was also constructed for the MPL where the porosity is 0.55 and the sphere radius is 80nm, both representative values for realistic MPLs.

Effect of crack length with fixed aperture

In the previous section, a set of symmetrical geometries were constructed where the aperture of the crack was held constant and the depth of the cracks were varied to span a quarter, a half, two thirds and the full length of the CL. It was observed that breakthrough occurred earlier and with lower saturation with elongated cracks, indicating that the porous regions which would be electrochemically active in a realistic case, would be free of water when the water is removed by the GDL. The short interfacial crack has high saturation at breakthrough meaning that when the water is removed by the GDL, the electrochemical area would be flooded by water.

In order to investigate how much of the effect can be attributed to the larger void volume of the longer cracks, corresponding to lower pore pressure and enhanced liquid water transport, we examine geometries with fixed volume of the perforation and vary the protrusion of the crack in the following section.

Effect of crack protrusion

A discussed in section 3.4, interfacial holes and dents at the interface of the CL and MPL can occupy as much volume as the elongated cracks that span the depth of the CL or MPL. However, it is speculated that interfacial structures and elongated cracks have very different effects on water transport, hence to study the effect of degree of protrusion into

the length of the layers, the volume is kept constant and the shape of the crack was varied from short and wide to thin and long.

The cracks were implemented in the CL and the MPL in separate experiments and can be visualized in figures 5.6 and 5.7. In both cases, the layer which is perforated has a volume of $8\mu m^3$ and the cracks have a volume of $0.4\mu m^3$ which is 5% of the volume of the layer, and stem from the interface. When the CL is non perforated, it takes $t = 75000\delta$ for water to reach the CL|MPL interface, therefore when studying the cracks in the MPL a shorter CL of 400nm in length was used to maintain the interfacial effects but have water reach the interface much sooner to study its behaviour in the MPL.

The total computational size of for the geometries with cracked CLs and MPLs are $2\mu m \times 4\mu m \times 2\mu m$ and $2\mu m \times 2.4\mu m \times 2\mu m$ respectively. Since the elongated cracks have a slab shape as opposed to a pinhole, the length of the crack in the z direction was fixed, and the length of the cracks in the x and y direction were varied across all geometries. The dimensions of the cracks and the associated visual representation are presented in table 5.1.

Table 5.1: Geometry of the cracks, listed in order of least protruded (short and wide) to the most protruded (long and thin) into the CL.

Depth of protrusion	Shown in figures	Dimension of the perforation (x, y z)
$0.5\mu m$	5.6b and 5.7b	$0.8\mu m \times 0.5\mu m \times 1\mu m$
$1\mu m$	5.6c and 5.7c	$0.4\mu m \times 1\mu m \times 1\mu m$
$1.5\mu m$	5.6d and 5.7d	$0.267\mu m \times 1.5\mu m \times 1\mu m$
$0.5\mu m$	5.6e and 5.7e	$0.2\mu m \times 2\mu m \times 1\mu m$

For the experiments with the cracks in the catalyst layer (geometries in figure 5.6), the evolution of saturation can be observed in figure 5.8. Compared to the simulation with no cracks, the water uptake is increased with the presence of the interfacial crack, even prior to the water reaching the crack. This suggests that despite being $1.5\mu m$ from the large perforation, the liquid water is influenced by the low pressure of the perforation. A visualization of water transport with the full length crack in the CL (figure 5.6e) is shown

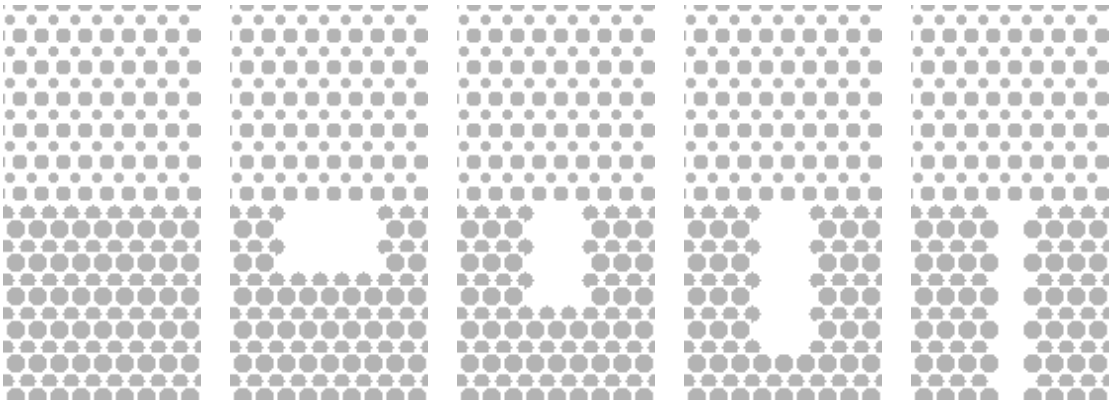

(a) (b) (c) (d) (e)

Figure 5.6: Slices of symmetrically constructed CL (bottom half) and MPL (top half) geometries with perforated cracks in the CL of constant volume and varying degree of protrusion. The depth of the perforations along the direction of the flow, the y axis, are (a) 0μm, (b) 0.5μm, (c) 1μm, (d) 1.5μm, and (e) 2μm. The total geometry has dimensions 2 μm × 4 μm × 2 μm.

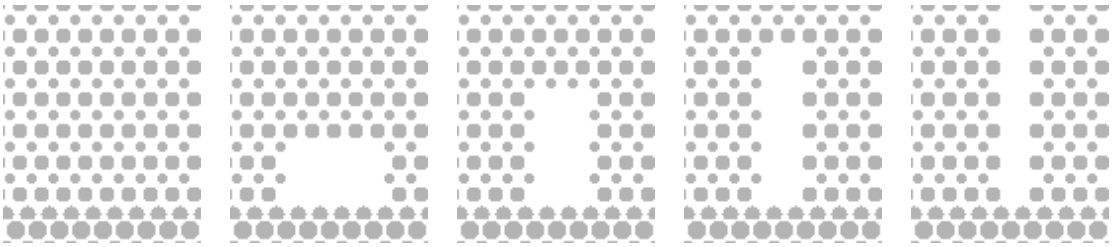

(a) (b) (c) (d) (e)

Figure 5.7: Slices of symmetrically constructed CL (bottom 17% of the layer) and MPL (top) geometries with perforated cracks in the MPL of constant volume and varying degree of protrusion. The depth of the perforations along the direction of the flow, the y axis, are (a) 0μm, (b) 0.5μm, (c) 1μm, (d) 1.5μm, and (e) 2μm. The total geometry has dimensions 2 μm × 2.4 μm × 2 μm.

in figure 5.9. The crack in the CL not only keeps porous regions around the crack free from flooding, but also creates a focused injection point into the MPL which leaves large areas clear from water which encourages gas mixing.

The evolution of saturation for the experiments with the cracks in the microporous layer (geometries in figure 5.7), is shown in figure 5.10. Since the domain is shorter, all geometries reaches breakthrough. The longer and thinner geometries achieve breakthrough

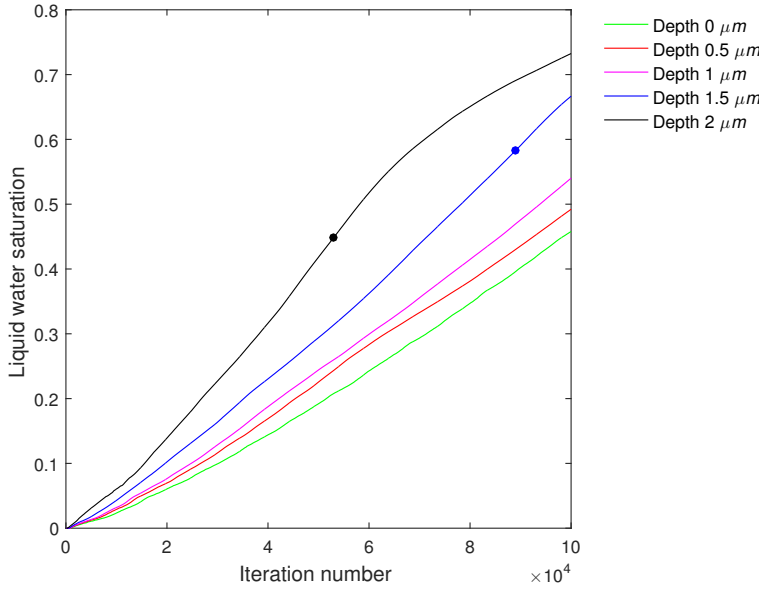

Figure 5.8: Evolution of saturation for a fixed crack volume and varying degrees of protrusion in the CL. The two of the geometries reached breakthrough, as indicated by the markers.

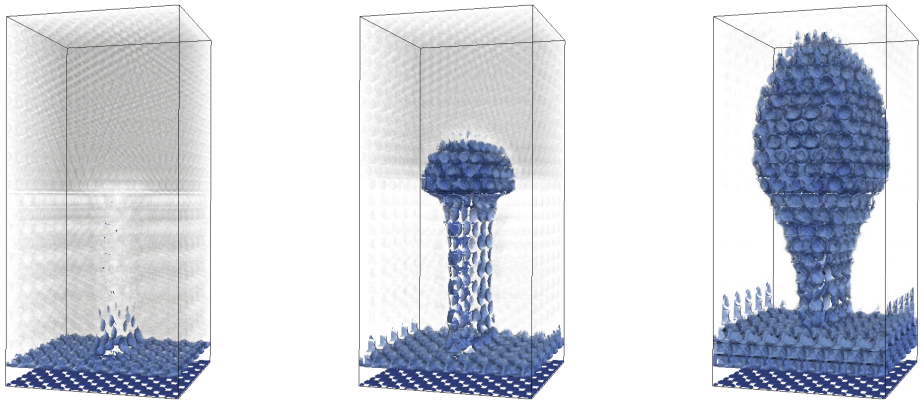

(a) $t = 7000\delta$ (b) $t = 20000\delta$ (c) $t = 50000\delta$

Figure 5.9: Water transport in a crack spanning the length of the CL. The breakthrough point occurs at $t = 50000\delta$.

first with significantly lower saturation, however after all geometries reach breakthrough and when $t = 100000\delta$ have passed, the amount liquid water saturation is larger for the shorter and larger cracks despite all cracks having the same void volume. This can be explained by the effective capillary pressure, the difference between the pressure of the liquid and gas phase. The capillary pressure at $t = 100000\delta$ for the cracks protruding

0.5μm, 1μm, 1.5μm and 2μm into the system are 0.0848 atm, 0.1933 atm, 0.3488 atm, and 0.5973 atm respectively.

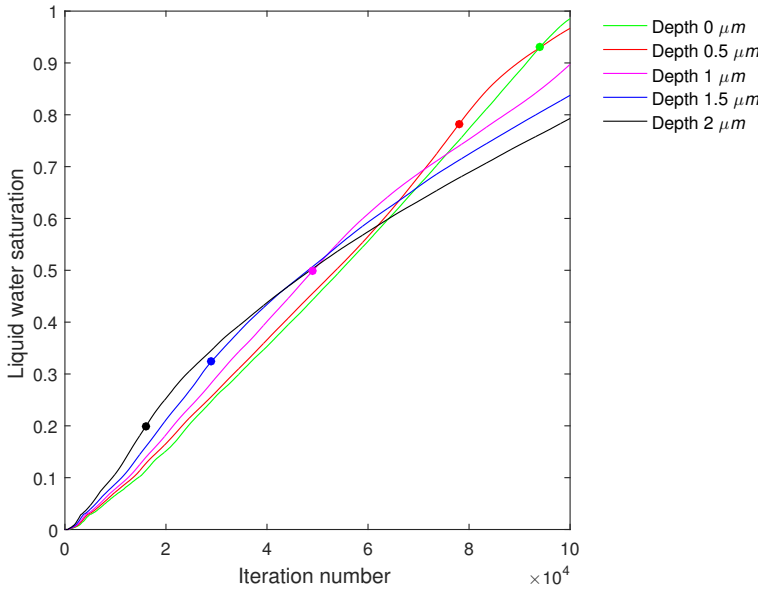

Figure 5.10: Evolution of saturation for a fixed crack volume and varying degrees of protrusion in the MPL. The breakthroughs are indicated by the markers.

The high capillary pressure in the system with the elongated crack can be explained by water pressure building up in the crack since it is a preferential path, and creating a large pressure difference between the phases. After it reaches breakthrough, the pressure in the crack is too large to encourage much more water uptake, but the water can continue to enter slowly in the high pressure capillary pores. This would encourage some water to move towards the membrane while also mitigating flooding.

In the short cracks, the water transport across the layer which is driven by an applied pressure gradient is slowed down by the presence of a large pore with low capillary pressure. To reach the end of the layer, the water must flow through the small pores which increases the pressure of the gas and lowers the liquid water pressure, reducing the average capillary pressure of the system. Since low capillary pressures encourage liquid water uptake, the cracks with a lower degree of protrusion will take up a larger amount of water after breakthrough. In much larger pores interfacial pores, the low pressure could counteract or

be stronger than the pressure gradient. In this case much more water would accumulate in the void before enough pressure is build to move through the pores, leading to liquid water pooling.

These results corroborate the experimental study conducted by Gerteisen et al. [16] where large straight perforations were introduced to a GDL using laser beams. They also observed reduced saturation at high current densities, in the range limited by mass transport. Their experiments showed that this improvement on water transport resulted in a higher limiting current density as well as a better overall performance of the test cell with the perforated GDL.

Effect of tortuosity

A degree of tortuosity is observed in long and thin cracks as presented in figure 3.2, and the effect of tortuosity on water transport is explored. The tortuous shapes were created using the same geometries as in the previous section, however creating new cracks by taking away spheres at certain angles in the MPL and CL. Since taking away spheres made for a cleaner cut when the slope was aligned with the nodes of the hexagonal close-packed (hcp) lattice, the slope of the perforation is different in the CL and MPL. Tortuosity is defined as the ratio of the length of the curve to the distance between the ends. The slope of the tortuous crack which is displayed in figure 5.11c in the CL is 1.5, yielding a tortuosity of 1.20. The constructed tortuous crack in the MPL is shown in 5.12c and has a slope of 1, which yields a tortuosity of 1.41.

The evolution of saturation for the experiments is shown in figure 5.13 for the cracked CL and in figure 5.14 for the cracked MPL. In both experiments, the breakthrough of the tortuous cracks occurs later and with slightly higher saturation than for the straight crack, suggesting that the higher tortuosity slightly reduces the water management benefits of elongated cracks.

Again, the shorter domain offered by the system with cracks in the MPL allows us to see how the systems behave after breakthrough. As can be observed from figure 5.14, the crack with tortuosity of 1.41 has higher liquid saturation after $t = 100000\delta$ compared to the crack with tortuosity of 1. The effective capillary pressure after $t = 100000\delta$ for the cracks of tortuosity 1 and 1.41 in the MPL are 0.5973 atm and 0.3815 atm respectively, suggesting that the straight crack is a more preferential path as water primarily passes through the perforation and builds up pressure, creating a large pressure difference between the phases and discouraging entry of water into the porous region. In the case of the tortuous crack, due to the inertia of the water and the pressure gradient not always being aligned with the direction of the perforation, a portion of the water strays from the path and the pressure in the crack is reduced as water flows between the solid spheres. This allows the system to uptake more water after breakthrough, as supported by the lower effective capillary pressure of the system.

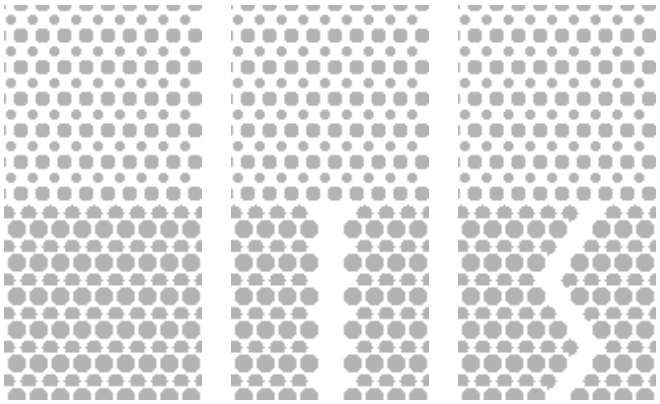

(a) (b) (c)

Figure 5.11: Slices of symmetrically constructed CL (bottom) and MPL (top) geometries with perforated cracks of constant volume and varying degree of tortuosity. The CL in (a) has no perforation, and the tortuosity of the perforations along the direction of the flow, the y axis, are (b) 1 , (c) 1.20.

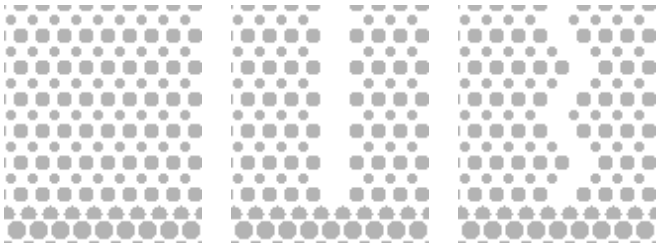

(a) (b) (c)

Figure 5.12: Slices of symmetrically constructed CL (bottom) and MPL (top) geometries with perforated cracks of constant volume and varying degree of tortuosity. The MPL in (a) has no perforation, and the tortuosity of the perforations along the direction of the flow, the y axis, are (b) 1 , (c) 1.41.

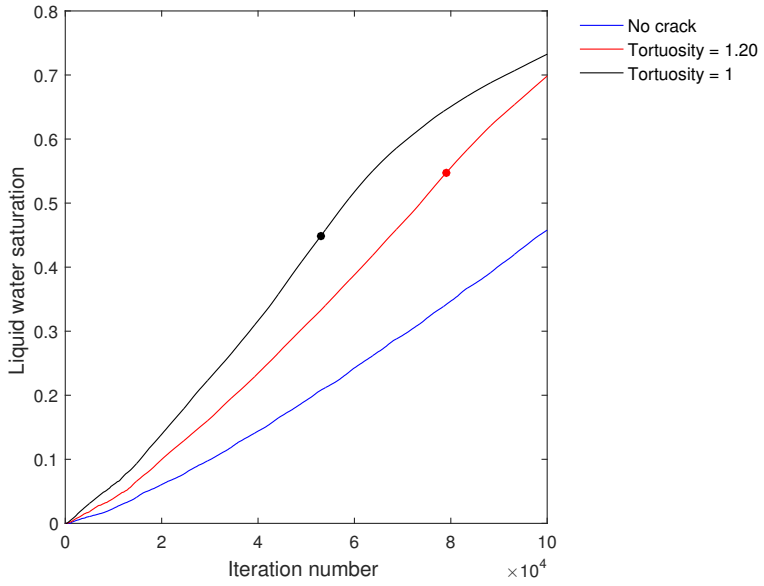

Figure 5.13: Evolution of saturation for a fixed crack volume and varying tortuosity in the MPL. The breakthroughs are indicated by the markers.

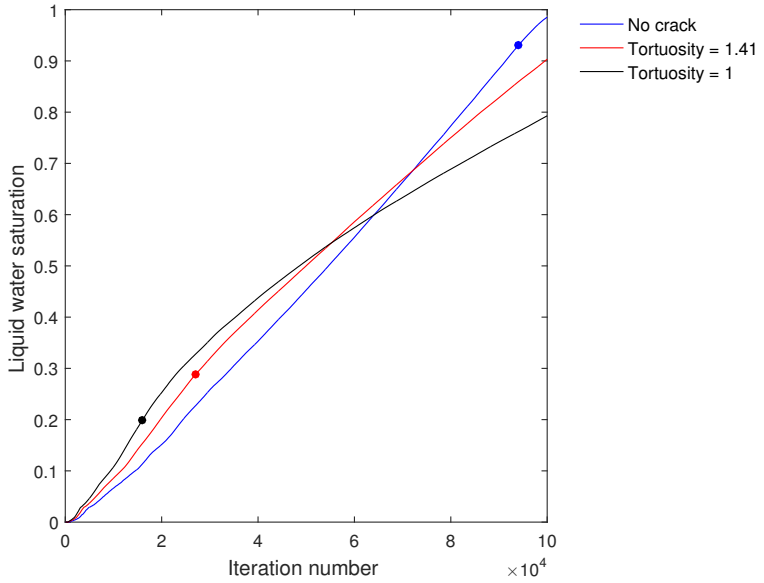

Figure 5.14: Evolution of saturation for a fixed crack volume and varying tortuosity in the CL. The breakthroughs are indicated by the markers.

5.3 Effect of catalyst layer cracks on transport properties

As discussed in section 3.3, cracks not only influence liquid water transport, but also gas diffusivity and conductivity due to a reduction in contact area. In order to study the effect of perforations on other transport properties such as oxygen and water vapour diffusion, electron and proton conductivity, and thermal conductivity, the pore scale model is coupled with the lattice Boltzmann model. The pore scale model takes as input a geometry with information on five phases including gas, carbon, platinum, ionomer and liquid water. The initial geometry used in this process was obtained with the method described in section 4.2.2 and is presented in figure 4.3. The geometry has dimensions 4.7 µm × 6.1 µm × 5.04 µm.

For the dry geometry used as a starting point to the the lattice Boltzmann model, the information on four phases obtained from the reconstructed CL (carbon, ionomer, gas and platinum) was reduced to two phases (gas and solid). Water was dispersed throughout the catalyst layer as described in the previous section such that liquid water saturation was 0.25

in the catalyst layer. A computationally generated MPL with random distribution of carbon spheres of radius 4 and of porosity 0.6 was appended to the end of the CL to remove the water and avoid accumulation of water at the boundary during the lattice Boltzmann simulation.

In this experiment, the cracks with constant volume and varying degree of protrusion are used, however the larger geometry allowed for larger cracks. The CL has a volume of $8\mu m^3$, and the cracks have a volume of $0.4\mu m^3$ which is 5% of the volume of the layer, as in the previous experiments. The dimensions of the perforated pores from the least protruded to the most protruded into the CL are indicated in table 5.2.

Note that the perforated volumes are equal for each geometry, however the random structure of the reconstructed CL can lead to large pores connected to the volume which adds uncertainty to the effective crack volume.

The gas transport in the pore scale model is driven by a difference in concentrations at opposite boundaries, therefore the liquid water distribution for this experiment can not be obtained from a percolation study as in the previous section because the constant influx of water at the boundary would interfere with gas transport.

A realistic model for water transport in the cathode would include water production in the catalyst layer. It would ideally be responsive to the amount of water and connectivity of pores to represent a reduction of chemical reaction rates under flooding conditions. As an exploratory step towards such a model, water was dispersed through the cathode and the water transport was modelled with no regeneration of water in appendix B. The results are preliminary, but the water distribution after $t = 3000\delta$ is obtained for this experiment using the technique outlined in appendix B and the reconstructed geometry described above.

A visualization of the water distribution after $t = 3000\delta$ is provided in figure 5.15 and the saturation levels at that time are listed in table 5.2. It should be noted that the liquid saturation in the crack of protrusion depth $1.2\mu m$ is larger than in the geometry with

no cracks, suggesting that liquid water has accumulated in the interfacial gap and it has hindered water management. The water distribution information at $t = 3000\delta$ was merged with the original dry geometry containing information on ionomer, platinum, carbon and gas and used as input to the pore scale model.

Table 5.2: Liquid water saturation at $t = 3000\delta$ for each geometry, listed in order of least protruded (short and wide) to the most protruded (long and thin) into the CL.

Liquid saturation at $t = 3000\delta$	Dimension of the perforation (x, y z)
0.1569	$0\mu m \times 0\mu m \times 0\mu m$
0.1537	$0.8\mu m \times 1.2\mu m \times 1.4\mu m$
0.1517	$0.4\mu m \times 2.6\mu m \times 1.4\mu m$
0.1519	$0.28\mu m \times 3.9\mu m \times 1.4\mu m$
0.1485	$0.2\mu m \times 5.2\mu m \times 1.4\mu m$

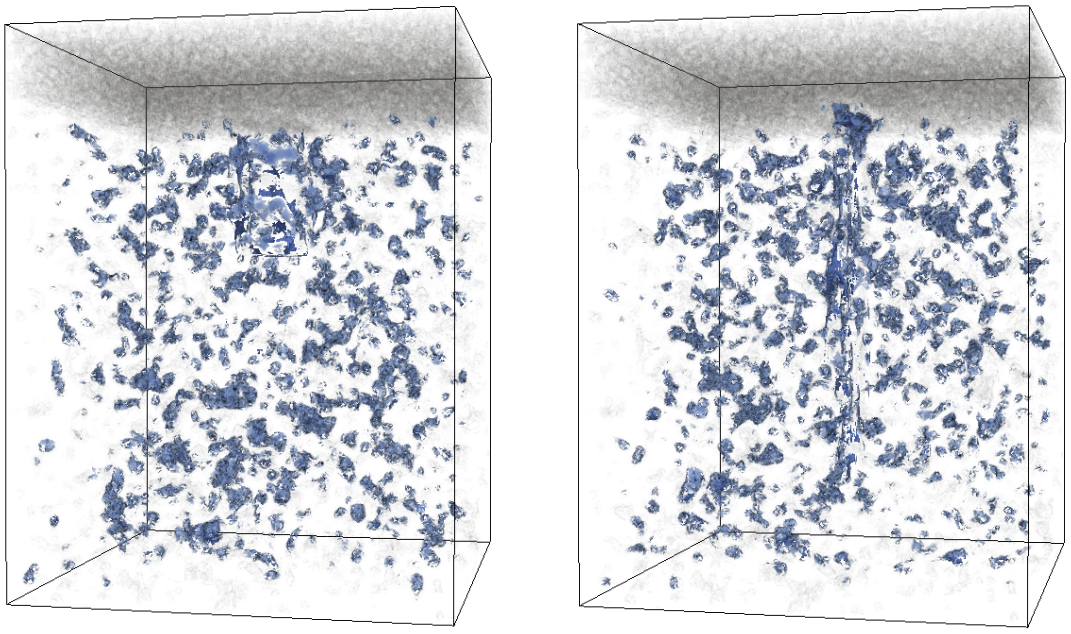

(a) 1.2µm protrusion depth of perforation, $t = 3000\ \delta$

(b) 5.2µm protrusion depth of perforation, $t = 3000\ \delta$

Figure 5.15: Water distribution in the merged layers for two crack morphologies at 3000δ.

To accentuate the effect of the liquid water on gas transport, the perforated geometries

described in table 5.2 with no liquid water were also used as input to the pore scale model.

The effective diffusivity of gases is presented as a function of the depth of protrusion of the perforation in figure 5.16. For the dry samples, the oxygen and water vapour diffusion increase steadily with the depth of protrusion. The wet sample does provide an increase in diffusion, suggesting that since the water does not completely fill the crack, they offer a preferential path for oxygen and water vapour as well. Note that the liquid saturation for these structures are very low as indicated in table 5.2, and in flooding conditions the pores may be completely blocked, reducing gas diffusion. Under wet conditions, the geometry with the most protruded perforation showed a similar increase in diffusivity when compared to the dry geometry which shows that when liquid water removal is effective, enhanced gas transport is achievable.

The impact of perforations on effective electron and proton conductivity are shown in figure 5.17. The decrease in conductivity across all cracked geometries are largely due to an increase in contact resistance. This loss could be tolerated in fuel cells operating at high power density where flooding would cause losses in electrochemical activity and the benefits of water management due to elongated cracks could outweigh the losses associated with contact resistance.

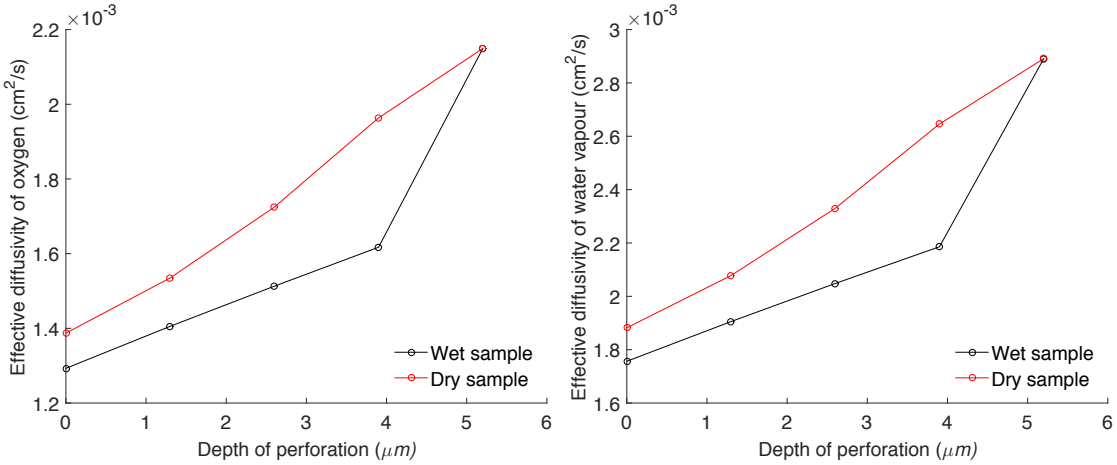

(a) Oxygen diffusivity (b) Water vapour diffusivity

Figure 5.16: Effective gas diffusivity with mass flow in the y direction.

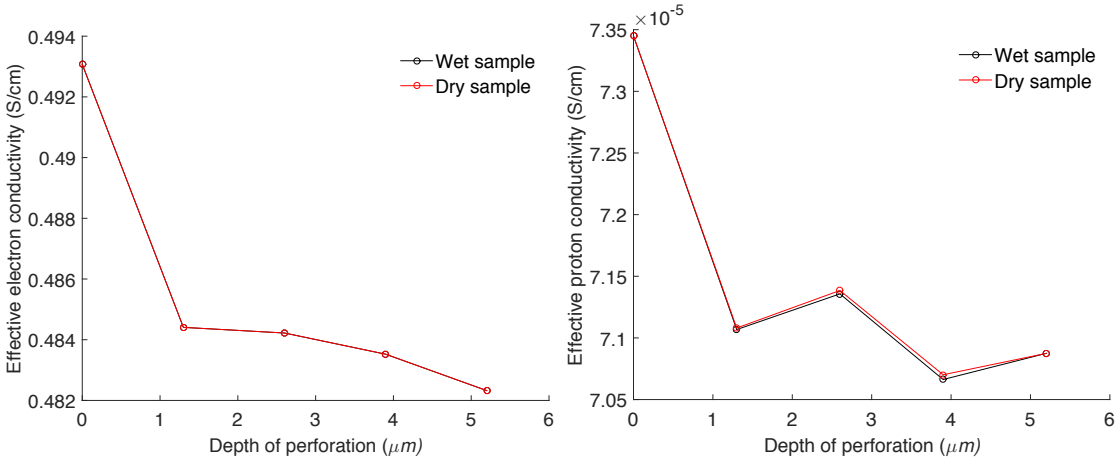

(a) Electron conductivity (b) Proton conductivity

Figure 5.17: Effective proton diffusivity with mass flow in the y direction.

Chapter 6

Conclusions and future work

6.1 Conclusions

This thesis contributes to the understanding of liquid water transport in fuel cell cathodes and in particular on the impact of morphological imperfections that are typical of physical cathodes: cracks and interfacial protrusions. Prior work in the Energy Systems and Transport Phenomena Lab at the University of Victoria had focused on LBM and pore scale modelling of catalyst layers. Building on this, in this thesis we examine for the first time the effect of cracks in a composite layer with a catalyst layer and microporous layer using the three dimensional LBM and pore scale model methodologies.

A multiple relaxation time lattice Boltzmann method (MRT-LBM) was used to study the effect of select crack characteristics on liquid water transport in the catalyst layer and microporous layer using a drainage process. To isolate the effect of the cracks from other large pores, symmetrically constructed layers were implemented. The increase in the crack aperture increased liquid water uptake proportionally with the area of the base of the crack, and water in tortuous cracks reached breakthrough slightly later than water in the straight crack. Perforations with constant volume and varied protrusion depths into the layer es-

sentially compared large interfacial gaps or holes to thin elongated cracks of equal volume. Elongated cracks allowed for faster breakthrough and lower saturation levels. The experiments are consistent with our understanding of how capillary pressure affects gas and liquid water transport.

A notable observation is that short and large interfacial cracks have a high potential of liquid water uptake due to the lower effective capillary pressures, however it does not lead to an increase in water management. Elongated cracks in the direction of the pressure gradient are a preferential pathway for liquid water and since less water strays from the path to travel through small pores, the capillary pressure increases which simultaneously encourages water to move towards the membrane and mitigates flooding. The large pressure of water in elongated cracks also allow for a large breakthrough pressure, thus providing effective injection sites into the subsequent layer of the cathode.

Additionally, gas diffusion as well as electron and proton conductivities were modelled in geometries with cracks of varying degrees of protrusion and a liquid water distribution which was obtained from the lattice Boltzmann method. A volume of liquid water was dispersed across the cracked geometries and modelled using the lattice Boltzmann simulation. The water distribution after $t = 3000\delta$ was used as input to the pore scale model to measure other transport properties. The effective diffusivity increased for all crack protrusion depths, even for the wet catalyst layer, likely due to low liquid water saturation. The geometry with the most elongated crack showed a significant increase in gas diffusion under wet conditions, showing that when liquid water removal is effective, enhanced gas transport is achievable. The proton and electron conductivities decreased for all crack shapes due to an increase in contact resistance.

6.2 Future work

Simulations that are completely representative of the water transport process in a fuel cell during operation would require coupling of the LBM model with distributed water generation at the local reaction sites within the catalyst layer. Preliminary simulations in this direction were presented in appendix B and issues regarding the ability of the MRT-LBM to model phase change were discussed. Further work is needed to systematically couple the simulations with electrochemistry and to incorporate appropriate modelling of phase change kinetics.

In this work, the interface between the porous layers was perfect, meaning it was smooth and there was no overlap region where both components of the CL and the MPL could be found. For a more realistic representation of interfacial morphologies in the cathode, an imperfect interface should be created, and a larger computational domain should be used.

Furthermore, the effect of water on the conductivity of the ionomer was also neglected, but should be modelled to further our understanding of the influence of water in the cathode.

Bibliography

[1] FE Hizir, SO Ural, EC Kumbur, and MM Mench. Characterization of interfacial morphology in polymer electrolyte fuel cells: Micro-porous layer and catalyst layer surfaces. *Journal of Power Sources*, 195(11):3463–3471, 2010.

[2] Sebastian Prass, Sadegh Hasanpour, Pradeep Kumar Sow, André B Phillion, and Walter Mérida. Microscale x-ray tomographic investigation of the interfacial morphology between the catalyst and micro porous layers in proton exchange membrane fuel cells. *Journal of Power Sources*, 319:82–89, 2016.

[3] K. Lange, C. Misra, P. Sui, and N. Djilali. A numerical study on preconditioning and partitioning schemes for reactive transport in a pemfc catalyst layer. *Comput. Methods Appl. Mec.h Engrg.*, 200:905–916, 2010.

[4] K. Lange, P. Sui, and N. Djilali. Determination of effective transport propoerties in a pemfc catalys later using different reconstruction algorithms. *Journal of Power Sources*, 208:354–365, 2012.

[5] J. Edmonds, J. Clarke, J. Dooley, S. H. Kim, and S. J. Smith. Stabilization of co2 in a b2 world: insights on the roles of carbon capture and disposal, hydrogen, and transportation technologies. *Energy Economics*, 26(4):517 – 537, 2004.

[6] S Litster and G McLean. Pem fuel cell electrodes. *Journal of Power Sources*, 130(1):61–76, 2004.

[7] K. Lange, P. Sui, and N. Djilali. Pore scale modeling of a proton exchange membrane fuel cell catalist layer: Effects of water vapor and temperature. *Journal of Power Sources*, 196:3195–3203, 2011.

[8] Adam Z Weber, Rodney L Borup, Robert M Darling, Prodip K Das, Thomas J Dursch, Wenbin Gu, David Harvey, Ahmet Kusoglu, Shawn Litster, Matthew M Mench, et al. A critical review of modeling transport phenomena in polymer-electrolyte fuel cells. *Journal of The Electrochemical Society*, 161(12):F1254–F1299, 2014.

[9] J. H. Nam, K-J. Lee, G-S. Hwang, C-J. Kim, and M. Kaviany. Microporous layer for water morphology control in {PEMFC}. *International Journal of Heat and Mass Transfer*, 52(11–12):2779 – 2791, 2009.

[10] K. N. Kim, J. H. Kang, S. G Lee, and J. H. Nam. Lattice boltzmann simulation of liquid water transport in microporous and gas diffusion layers of polymer electrolyte membrane fuel cells. *Journal of Power Sources*, 278:703–717, 2015.

[11] Michael P Manahan, Soowhan Kim, Emin C Kumbur, and Matthew M Mench. Effects of surface irregularities and interfacial cracks on polymer electrolyte fuel cell performance. *ECS Transactions*, 25(1):1745–1754, 2009.

[12] F. Mack, M. Klages, J. Scholta, L. Jörissen, T. Morawietz, R. Hiesgen, D. Kramer, and R. Zeis. Morphology studies on high-temperature polymer electrolyte membrane fuel cell electrodes. *Journal of Power Sources*, 255:431 – 438, 2014.

[13] R. Banan, A. Bazylak, and J. Zu. Combined effects of environmental vibrations and hygrothermal fatigue on mechanical damage in pem fuel cells. *International Journal of Hydrogen Energy*, 40(4):1911–1922, 2015.

[14] R Banan, J Zu, and A Bazylak. Humidity and temperature cycling effects on cracks and delaminations in pemfcs. *Fuel Cells*, 15(2):327–336, 2015.

[15] H. Markötter, .R Alink, J. Haußmann, K. Dittmann, T. Arlt, F. Wieder, C. Tötzke, M. Klages, C. Reiter, H. Riesemeier, et al. Visualization of the water distribution in perforated gas diffusion layers by means of synchrotron x-ray radiography. *International Journal of Hydrogen Hnergy*, 37(9):7757–7761, 2012.

[16] D Gerteisen, T Heilmann, and C Ziegler. Enhancing liquid water transport by laser perforation of a gdl in a pem fuel cell. *Journal of Power Sources*, 177(2):348–354, 2008.

[17] M. Manahan and M. Mench. Increased performance of pefcs with engineered mass-transport pathways. *ECS Transactions*, 41(1):569–581, 2011.

[18] B. Han and H. Meng. Numerical studies of interfacial phenomena in liquid water transport in polymer electrolyte membrane fuel cells using the lattice boltzmann method. *International Journal of Hydrogen Energy*, 38:5053–5059, 2013.

[19] X-D. Niu, T. Munekata, S-A. Hyodo, and K. Suga. An investigation of water-gas transport processes in the gas-diffusion-layer of a pem fuel cell by a multi-phase multiple-relaxation-time lattice boltzmann model. *Journal of Power Sources*, 172(2):542–552, 2007.

[20] Toshikazu Kotaka, Yuichiro Tabuchi, and Partha P Mukherjee. Microstructural analysis of mass transport phenomena in gas diffusion media for high current density operation in pem fuel cells. *Journal of Power Sources*, 280:231–239, 2015.

[21] Sukkee Um and Chao-Yang Wang. Computational study of water transport in proton exchange membrane fuel cells. *Journal of Power Sources*, 156(2):211–223, 2006.

[22] Matthew M Mench. *Fuel cell engines*. John Wiley & Sons, 2008.

[23] Rod Borup, Jeremy Meyers, Bryan Pivovar, Yu Seung Kim, Rangachary Mukundan, Nancy Garland, Deborah Myers, Mahlon Wilson, Fernando Garzon, David Wood,

et al. Scientific aspects of polymer electrolyte fuel cell durability and degradation. *Chemical reviews*, 107(10):3904–3951, 2007.

[24] Hua Meng and Chao-Yang Wang. Model of two-phase flow and flooding dynamics in polymer electrolyte fuel cells. *Journal of the Electrochemical Society*, 152(9):A1733–A1741, 2005.

[25] Hui Li, Yanghua Tang, Zhenwei Wang, Zheng Shi, Shaohong Wu, Datong Song, Jianlu Zhang, Khalid Fatih, Jiujun Zhang, Haijiang Wang, et al. A review of water flooding issues in the proton exchange membrane fuel cell. *Journal of Power Sources*, 178(1):103–117, 2008.

[26] Jingwei Hu, PC Sui, Sanjiv Kumar, and Ned Djilali. Modelling and simulations of carbon corrosion during operation of a polymer electrolyte membrane fuel cell. *Electrochimica Acta*, 54(23):5583–5592, 2009.

[27] F Bresciani, A Casalegno, G Varisco, and R Marchesi. Water transport into pefc gas diffusion layer: experimental characterization of diffusion and permeation. *International Journal of Energy Research*, 38(5):602–613, 2014.

[28] Antoni Forner-Cuenca, Johannes Biesdorf, Lorenz Gubler, Per Magnus Kristiansen, Thomas Justus Schmidt, and Pierre Boillat. Engineered water highways in fuel cells: Radiation grafting of gas diffusion layers. *Advanced Materials*, 27(41):6317–6322, 2015.

[29] S Shimpalee, U Beuscher, and JW Van Zee. Analysis of gdl flooding effects on pemfc performance. *Electrochimica Acta*, 52(24):6748–6754, 2007.

[30] J Lee, R Yip, P Antonacci, N Ge, T Kotaka, Y Tabuchi, and A Bazylak. Synchrotron investigation of microporous layer thickness on liquid water distribution in a pem fuel cell. *Journal of The Electrochemical Society*, 162(7):F669–F676, 2015.

[31] Adam Z Weber and John Newman. Effects of microporous layers in polymer electrolyte fuel cells. *Journal of the Electrochemical Society*, 152(4):A677–A688, 2005.

[32] Zhigang Qi and Arthur Kaufman. Improvement of water management by a microporous sublayer for pem fuel cells. *Journal of Power Sources*, 109(1):38–46, 2002.

[33] Enju Nishiyama, Masaya Hara, and Toshiaki Murahashi. Role of the cathode microporous layer in a pemfc. *ECS Transactions*, 50(2):569–580, 2013.

[34] Xiaoxian Zhang, Yuan Gao, Hossein Ostadi, Kyle Jiang, and Rui Chen. Modelling water intrusion and oxygen diffusion in a reconstructed microporous layer of pem fuel cells. *International Journal of Hydrogen Energy*, 39(30):17222–17230, 2014.

[35] T Berning and N Djilali. A 3d, multiphase, multicomponent model of the cathode and anode of a pem fuel cell. *Journal of the Electrochemical Society*, 150(12):A1589–A1598, 2003.

[36] N Djilali. Computational modelling of polymer electrolyte membrane (pem) fuel cells: challenges and opportunities. *Energy*, 32(4):269–280, 2007.

[37] Jingsheng Ma, Xiaoxian Zhang, Zeyung Jiang, Hossein Ostadi, Kyle Jiang, and Rui Chen. Flow properties of an intact mpl from nano-tomography and pore network modelling. *Fuel*, 136:307–315, 2014.

[38] EF Medici and JS Allen. The effects of morphological and wetting properties of porous transport layers on water movement in pem fuel cells. *Journal of The Electrochemical Society*, 157(10):B1505–B1514, 2010.

[39] Chiyu Xie, Ali Q Raeini, Yihang Wang, Martin J Blunt, and Moran Wang. An improved pore-network model including viscous coupling effects using direct simulation by the lattice boltzmann method. *Advances in Water Resources*, 100:26–34, 2017.

[40] X. Shan and H. Chen. Simulation of nonideal gases and liquid-gas phase transitions by the lattice boltzmann equation. *Phys. Rev. E*, 49:2941–2948, Apr 1994.

[41] Michael R Swift, E Orlandini, WR Osborn, and JM Yeomans. Lattice boltzmann simulations of liquid-gas and binary fluid systems. *Physical Review E*, 54(5):5041, 1996.

[42] Haihu Liu, Qinjun Kang, Christopher R Leonardi, Sebastian Schmieschek, Ariel Narváez, Bruce D Jones, John R Williams, Albert J Valocchi, and Jens Harting. Multiphase lattice boltzmann simulations for porous media applications. *Computational Geosciences*, 20(4):777–805, 2016.

[43] Xiaowen Shan and Hudong Chen. Lattice boltzmann model for simulating flows with multiple phases and components. *Physical Review E*, 47(3):1815, 1993.

[44] Shohji Tsushima and Shuichiro Hirai. An overview of cracks and interfacial voids in membrane electrode assemblies in polymer electrolyte fuel cells. *Journal of Thermal Science and Technology*, 10(1):JTST0002–JTST0002, 2015.

[45] M Oszcipok, D Riemann, U Kronenwett, M Kreideweis, and M Zedda. Statistic analysis of operational influences on the cold start behaviour of pem fuel cells. *Journal of power sources*, 145(2):407–415, 2005.

[46] Yanling Qiu, Hexiang Zhong, Meiri Wang, and Huamin Zhang. Effect of relative humidity cycles accompanied by intermittent start/stop switches on performance degradation of membrane electrode assembly components in proton exchange membrane fuel cells. *Journal of Power Sources*, 283:171–180, 2015.

[47] Xinyu Huang, Roham Solasi, YUE Zou, Matthew Feshler, Kenneth Reifsnider, David Condit, Sergei Burlatsky, and Thomas Madden. Mechanical endurance of polymer

electrolyte membrane and pem fuel cell durability. *Journal of Polymer Science Part B: Polymer Physics*, 44(16):2346–2357, 2006.

[48] Z Fishman and A Bazylak. Heterogeneous through-plane porosity distributions for treated pemfc gdls. ii. effect of mpl cracks. *Journal of The Electrochemical Society*, 158(8):B846–B851, 2011.

[49] Chang Sun Kong, Do-Young Kim, Han-Kyu Lee, Yong-Gun Shul, and Tae-Hee Lee. Influence of pore-size distribution of diffusion layer on mass-transport problems of proton exchange membrane fuel cells. *Journal of Power Sources*, 108(1):185–191, 2002.

[50] Yusuke Aoyama, Kengo Suzuki, Yutaka Tabe, Takemi Chikahisa, and Toshihiro Tanuma. Water transport and pefc performance with different interface structure between micro-porous layer and catalyst layer. *Journal of the electrochemical society*, 163(5):F359–F366, 2016.

[51] Wei-Mon Yan, Dong-Kai Wu, Xiao-Dong Wang, Ai-Lien Ong, Duu-Jong Lee, and Ay Su. Optimal microporous layer for proton exchange membrane fuel cell. *Journal of Power Sources*, 195(17):5731–5734, 2010.

[52] Yoshiyuki Komoda, Ko Okabayashi, Hironobu Nishimura, Masashi Hiromitsu, Takanori Oboshi, and Hiromoto Usui. Dependence of polymer electrolyte fuel cell performance on preparation conditions of slurry for catalyst layers. *Journal of Power Sources*, 193(2):488–494, 2009.

[53] Makoto Uchida, Yuko Aoyama, Nobuo Eda, and Akira Ohta. Investigation of the microstructure in the catalyst layer and effects of both perfluorosulfonate ionomer and ptfe-loaded carbon on the catalyst layer of polymer electrolyte fuel cells. *Journal of the Electrochemical Society*, 142(12):4143–4149, 1995.

[54] Takahiro Suzuki, Ryohei Hashizume, and Masanori Hayase. Effect of blending carbon nanoparticles and nanotubes on the formation of porous structure and the performance of proton exchange membrane fuel cell catalyst layers. *Journal of Power Sources*, 286:109–117, 2015.

[55] GW Horgan and IM Young. An empirical stochastic model for the geometry of two-dimensional crack growth in soil (with discussion). *Geoderma*, 96(4):263–276, 2000.

[56] Michael P Wnuk and Arash Yavari. A discrete cohesive model for fractal cracks. *Engineering Fracture Mechanics*, 76(4):548–559, 2009.

[57] AC Fowler and DR Scott. Hydraulic crack propagation in a porous medium. *Geophysical Journal International*, 127(3):595–604, 1996.

[58] Tushar Swamy, EC Kumbur, and MM Mench. Characterization of interfacial structure in pefcs: water storage and contact resistance model. *Journal of The Electrochemical Society*, 157(1):B77–B85, 2010.

[59] Minjeh Ahn, Yong-Hun Cho, Yoon-Hwan Cho, Jinho Kim, Namgee Jung, and Yung-Eun Sung. Influence of hydrophilicity in micro-porous layer for polymer electrolyte membrane fuel cells. *Electrochimica Acta*, 56(5):2450–2457, 2011.

[60] S Haase and M Rauber. Ex-situ gas diffusion layer intrusion effect determination of polymer electrolyte membrane fuel cell flow fields. *Journal of Power Sources*, 291:246–254, 2015.

[61] Michael J Martínez-Rodríguez, Tong Cui, Sirivatch Shimpalee, Supapan Seraphin, Binh Duong, and John W Van Zee. Effect of microporous layer on macmullin number of carbon paper gas diffusion layer. *Journal of Power Sources*, 207:91–100, 2012.

[62] R Singh, AR Akhgar, PC Sui, KJ Lange, and N Djilali. Dual-beam fib/sem characterization, statistical reconstruction, and pore scale modeling of a pemfc catalyst layer. *Journal of The Electrochemical Society*, 161(4):F415–F424, 2014.

[63] Alireza Akhgar. *Computational analysis of multi-phase flow in porous media with application to fuel cells*. PhD thesis, University of Victoria, 2016.

[64] Graeme Austin Bird. Molecular gas dynamics. *NASA STI/Recon Technical Report A*, 76, 1976.

[65] Dieter A Wolf-Gladrow. *Lattice-gas cellular automata and lattice Boltzmann models: an introduction*. Springer, 2004.

[66] Zhenhua Chai, Baochang Shi, and Zhaoli Guo. A multiple-relaxation-time lattice boltzmann model for general nonlinear anisotropic convection–diffusion equations. *Journal of Scientific Computing*, 69(1):355–390, 2016.

[67] Huina Li, Chongxun Pan, and Cass T Miller. Pore-scale investigation of viscous coupling effects for two-phase flow in porous media. *Physical Review E*, 72(2):026705, 2005.

[68] Abbas Fakhari and Diogo Bolster. Diffuse interface modeling of three-phase contact line dynamics on curved boundaries: A lattice boltzmann model for large density and viscosity ratios. *Journal of Computational Physics*, 334:620–638, 2017.

[69] David Jacqmin. Calculation of two-phase navier–stokes flows using phase-field modeling. *Journal of Computational Physics*, 155(1):96–127, 1999.

[70] Dominique d'Humières. Multiple–relaxation–time lattice boltzmann models in three dimensions. *Philosophical Transactions of the Royal Society of London A: Mathematical, Physical and Engineering Sciences*, 360(1792):437–451, 2002.

[71] W. G. Pollard and R. D. Present. On gaseous self-diffusion in long capillary tubes. *Phys. Rev.*, 73:162, 1948.

[72] R. E. Cunningham and RJJ Williams. *Diffusion in gases and porous media*. Springer, 1980.

[73] K. Lange, P. Sui, and N. Djilali. Pore scale simulation of transport and electrochemical reactions in reconstructed pemfc catalyst layers. *Journal of the Electrochemical Society*, 157:B1434–B1442, 2010.

[74] Sharonmoyee Goswami, Shannon Klaus, and Jay Benziger. Wetting and absorption of water drops on nafion films. *Langmuir*, 24(16):8627–8633, 2008.

[75] M Sabharwal, LM Pant, A Putz, D Susac, J Jankovic, and M Secanell. Analysis of catalyst layer microstructures: From imaging to performance. *Fuel Cells*, 16(6):734–753, 2016.

[76] Hesameddin Safari, Mohammad Hassan Rahimian, and Manfred Krafczyk. Extended lattice boltzmann method for numerical simulation of thermal phase change in two-phase fluid flow. *Physical Review E*, 88(1):013304, 2013.

Appendix A

Derivation of the Boltzmann equation

To arrive at the Boltzmann equation, we must make the assumption that the density of the matter is low such that only binary collisions can be considered.

Furthermore, for a system with N particles, we can express the number of particles in a physical and velocity space, dN as

$$dN = nf(\mathbf{u}, \mathbf{r}) d\mathbf{u} d\mathbf{r} \tag{A.1}$$

Deconvoluting the the collision mechanism will help construct the Boltzmann equation. Let's begin with an expression for the rate of change of the number of molecules in $d\mathbf{u}d\mathbf{r}$:

$$\Phi = \frac{\partial}{\partial t}(nf)\ d\mathbf{r}d\mathbf{u} \tag{A.2}$$

Next we consider how the number of molecules change in $d\mathbf{u}d\mathbf{r}$. First, we consider the molecules with velocity $\mathbf{u}$ moving through the physical space $d\mathbf{r}$. We can assume $\mathbf{u}$ be constant in $d\mathbf{r}$ by making the approximation that the spacial distribution function is constant over the small collision region. As shown by equation A.3 we start by expressing the flux of number of molecules, Φ across a surface dS of $d\mathbf{r}$, where $\mathbf{e}_r$ is the unit normal to dS,

with the intention of applying Gauss' Theorem in order to express the vector field inside the volume.

$$\Phi^u = -\int_S (\mathbf{u}\cdot\mathbf{e}_r) nf \, dS d\mathbf{u} \tag{A.3}$$

Next Gauss' theorem is applied, recalling that $d\mathbf{r}$ is the volume, therefore to integrate with respect to the volume, we use the volume element $d(d\mathbf{r})$. The rate of change of the number of molecules becomes

$$\Phi^u = -\int_{dr} \nabla\cdot(nf\mathbf{u}) \; d(d\mathbf{r}) d\mathbf{u}. \tag{A.4}$$

With further manipulation, keeping in mind that the divergence of $\mathbf{u}$, a constant over the spacial element, is 0.

$$\begin{aligned}
\Phi^u &= -\nabla\cdot(nf\mathbf{u}) \; d\mathbf{r}d\mathbf{u} \\
&= -[\nabla nf\cdot\mathbf{u} + nf(\nabla\cdot\mathbf{u})] \; d\mathbf{r}d\mathbf{u} \\
&= -\mathbf{u}\cdot\frac{\partial}{\partial\mathbf{r}}(nf) \; d\mathbf{r}d\mathbf{u}
\end{aligned} \tag{A.5}$$

Second, we take into account the effect of external forces on the velocity. The number of molecules with force $\mathbf{F} = m\dot{\mathbf{u}}$ moving across a surface dS of the physical space is

$$\Phi^F = -\int_S (\dot{\mathbf{u}}\cdot\mathbf{e}_r) nf \, dS d\mathbf{u}. \tag{A.6}$$

Similar mathematical as above yields the final yields

$$\Phi^F = -\frac{\mathbf{F}}{m}\cdot\frac{\partial}{\partial\mathbf{u}}(nf) \; d\mathbf{r}d\mathbf{u}. \tag{A.7}$$

Finally, assuming that the collision is instantaneous, the encounter causes a change

in the particles' velocity, with the position remaining unchanged. We will consider the collision between particles with velocity $\mathbf{u}$ and $\mathbf{u}_1$, $\mathbf{u}_r$ being the relative velocity of $\mathbf{u}$ with respect to $\mathbf{u}_1$, which have velocities $\mathbf{u}'$ and $\mathbf{u}_1'$ after the collision ($\mathbf{u}, \mathbf{u}_1 \rightarrow \mathbf{u}', \mathbf{u}_1'$).

The differential cross section between the particles after the collision is $\sigma d\Omega$, where σ is the cross section and Ω is the solid angle, so the volume this differential space occupies is $\mathbf{u}_r \sigma d\Omega$.

The number of particles of velocity $\mathbf{u}$ and $\mathbf{u}_1$ is $nf_1\mathbf{u}_1$ and $nf_1\mathbf{u}$ respectively. The number of $\mathbf{u}, \mathbf{u}_1 \rightarrow \mathbf{u}', \mathbf{u}_1'$ collisions are therefore

$$n^2 f f_1 \mathbf{u}_r \sigma d\Omega d\mathbf{u}_1 d\mathbf{ur}. \tag{A.8}$$

Let's now consider collisions producing particles with velocity $\mathbf{u}$ and $\mathbf{u}_1$, referred as inverse collisions, $\mathbf{u}', \mathbf{u}_1' \rightarrow \mathbf{u}, \mathbf{u}_1$. The mathematics is similar, and we keeping in mind that symmetry allows us to equate the differential cross sections and velocity space elements pre and post collision ($\sigma d\Omega d\mathbf{u}_1 d\mathbf{ur} = (\sigma d\Omega)' d\mathbf{u}_1' d\mathbf{u}'$) , the number of these collisions is

$$n^2 f' f_1' \mathbf{u}_r (\sigma d\Omega) d\mathbf{u}_1 d\mathbf{ur}. \tag{A.9}$$

Therefore the total rate of production of particles with velocity $\mathbf{u}$, integrated over all possible particles in $\mathbf{u}_1$, and solid angles is

$$\Phi^{collision} = \int_{-\infty}^{\infty} \int_{0}^{4\pi} n^2 (f' f_1' - f f_1) \mathbf{u}_r (\sigma d\Omega) d\mathbf{u}_1 d\mathbf{ur}. \tag{A.10}$$

Combining expressions A.2, A.5, A.7 and A.10 for the rate of change of the number of molecules in $d\mathbf{u}d\mathbf{r}$ for all the processes involved in the collision, we can obtain after some

manipulation the Boltzmann equation:

$$\frac{\partial}{\partial t}(nf) + \mathbf{u} \cdot \frac{\partial}{\partial \mathbf{r}}(nf) + \frac{\mathbf{F}}{m} \cdot \frac{\partial}{\partial \mathbf{u}}(nf) = \int_{-\infty}^{\infty} \int_{0}^{4\pi} n^2 (f' f_1' - f f_1) \mathbf{u}_r (\sigma d\Omega) d\mathbf{u}_1. \quad \text{(A.11)}$$

Appendix B

Evolution of water in the catalyst layer

As discussed at the beginning of chapter 5, a realistic model for water transport in the cathode would include water production in the catalyst layer. It would ideally be responsive to the amount of water and connectivity of pores to represent a reduction of chemical reaction rates under flooding conditions. As an exploratory step towards such a model, water was dispersed through the cathode and the water transport was modelled with no regeneration of water. The geometries used are the assembled CL and MPL structure with perforations in the CLs of constant volume and different degrees of protrusion shown in figure 5.6. To add water in the domain, a random number generator was used to find gas cells next to carbon spheres and replace them with water droplets to represent water being generated at the carbon interface. The process was repeated until liquid water saturation reached 0.25 in the catalyst layer.

As observed in the visualization in figure B.2 for water transport in an elongated crack, part of the water travels through the crack while a large fraction of the water changes phase as it travels through the pores.

The evolution of the water saturation is presented in figure B.3 for all crack morphologies. The saturation drop suggests liquid water changing phases as it travels through the

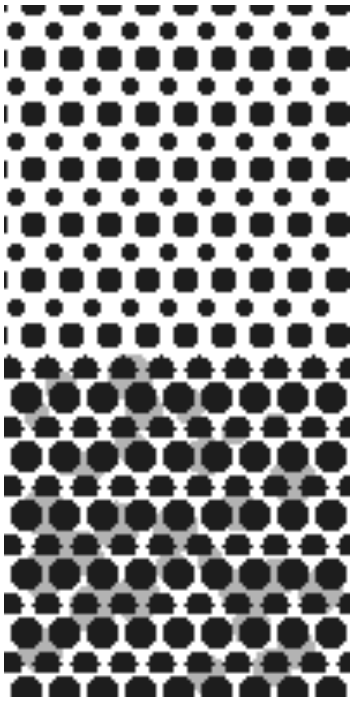

Figure B.1: Slice of the reconstructed geometry with no perforations and water computationally added until liquid water saturation reached 0.25 in the catalyst layer. The gas, liquid water and solid are represented by the shades white, grey and black respectively.

small pores as visualized in figure B.2. These results are to be viewed with caution because the MRT-LBM used in this study does not properly model phase change. Further work is needed to systematically couple the simulations with electrochemistry and to incorporate appropriate modelling of phase change kinetics [76].

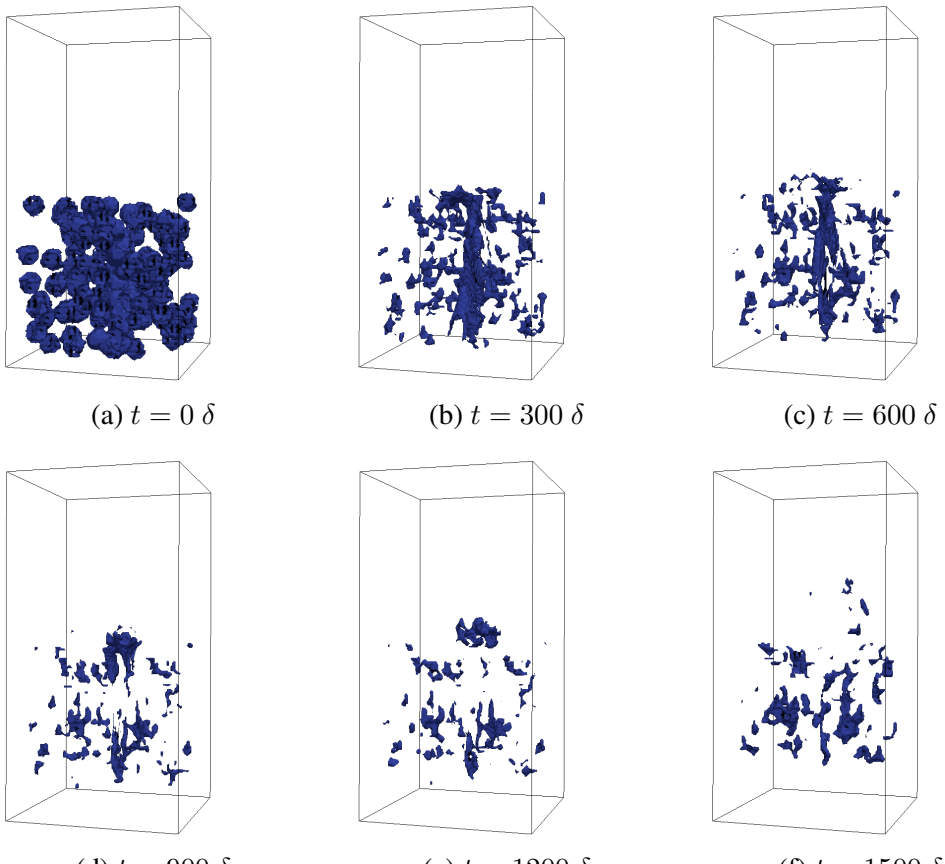

(a) $t = 0\ \delta$ (b) $t = 300\ \delta$ (c) $t = 600\ \delta$

(d) $t = 900\ \delta$ (e) $t = 1200\ \delta$ (f) $t = 1500\ \delta$

Figure B.2: Water transport through a symmetrically constructed CL(bottom half) and MPL(top half) geometry with an elongated crack spanning the length of the CL at intervals of 300s.

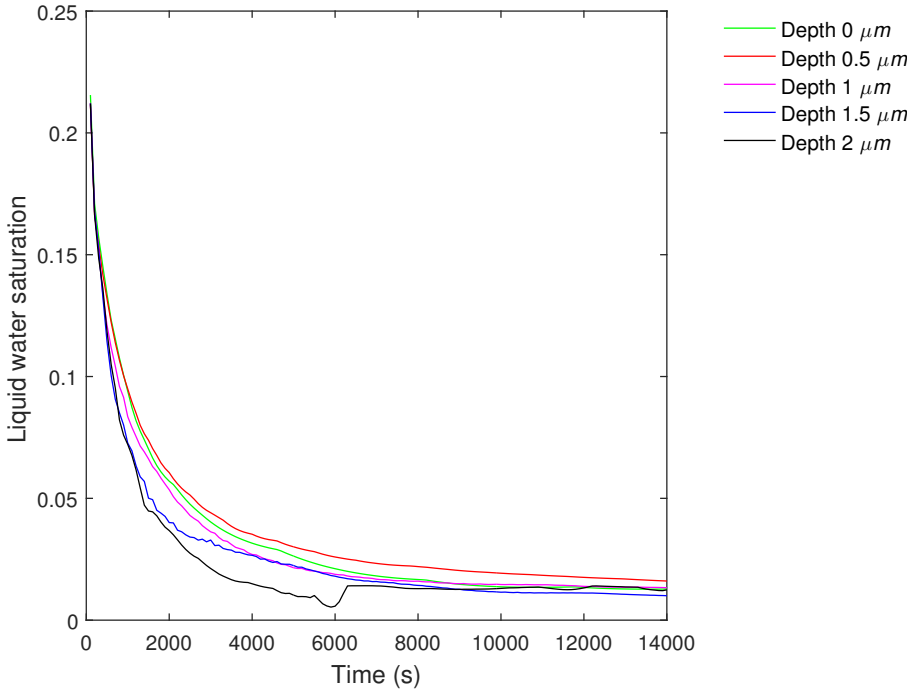

Figure B.3: Evolution of saturation for an elongated crack in the CL and an initial distribution of water.